

SAGITTARIUS A* ACCRETION FLOW AND BLACK HOLE PARAMETERS FROM GENERAL RELATIVISTIC DYNAMICAL AND POLARIZED RADIATIVE MODELING

ROMAN V. SHCHERBAKOV¹, ROBERT F. PENNA², JONATHAN C. MCKINNEY³

Draft version March 25, 2022

ABSTRACT

We obtain estimates of Sgr A* accretion flow and black hole parameters by fitting polarized sub-mm observations with spectra computed using three-dimensional (3D) general relativistic (GR) magnetohydrodynamical (MHD) (GRMHD) simulations. Observations are compiled from averages over many epochs from reports in 29 papers for estimating the mean fluxes F_ν , linear polarization (LP) fractions, circular polarization (CP) fractions, and electric vector position angles (EVPAs). GRMHD simulations are computed with dimensionless spins $a_* = 0, 0.5, 0.7, 0.9, 0.98$ over a $20,000M$ time interval. We perform fully self-consistent GR polarized radiative transfer using our new code to explore the effects of spin a_* , inclination angle θ , position angle (PA), accretion rate \dot{M} , and electron temperature T_e (T_e is reported for radius $6M$). By fitting the mean sub-mm fluxes and LP/CP fractions, we obtain estimates for these model parameters and determine the physical effects that could produce polarization signatures. Our best bet model has $a_* = 0.5$, $\theta = 75^\circ$, PA = 115° , $\dot{M} = 4.6 \times 10^{-8} M_\odot \text{year}^{-1}$, and $T_e = 3.1 \times 10^{10}$ K at $6M$. The sub-mm CP is mainly produced by Faraday conversion as modified by Faraday rotation, and the emission region size at 230 GHz is consistent with the VLBI size of $37\mu\text{as}$. Across all spins, model parameters are in the ranges $\theta = 42^\circ - 75^\circ$, $\dot{M} = (1.4 - 7.0) \times 10^{-8} M_\odot \text{year}^{-1}$, and $T_e = (3 - 4) \times 10^{10}$ K. Polarization is found both to help differentiate models and to introduce new observational constraints on the effects of the magnetic field that might not be fit by accretion models so-far considered.

Subject headings: accretion, accretion disks – black hole physics – Galaxy: center – radiative transfer – relativistic processes — polarization

1. INTRODUCTION

The mass of the Galactic Center black hole (BH) is $M \approx 4.5 \cdot 10^6 M_\odot$ (Ghez et al. 2008; Reid et al. 2008; Gillessen et al. 2009) and the spin is uncertain (Huang et al. 2009b; Broderick et al. 2009; Moscibrodzka et al. 2009; Broderick et al. 2010; Dexter et al. 2010). It resides at a distance $d \approx 8.4$ kpc. Because of its proximity, it has been observed in many wavelengths: γ -rays, X-rays, IR, (sub-)mm, and radio. X-ray bremsstrahlung emission originates from hot gas at large radii where the BH's gravity becomes important (Narayan, Yi & Mahadevan 1995; Narayan et al. 1998; Shcherbakov & Baganoff 2010) and Compton-scattered emission originates from close to the horizon (Moscibrodzka et al. 2009). X-rays at large radii are spatially resolved and have been used to constrain dynamical models for this region (Shcherbakov & Baganoff 2010). The sub-mm emission is cyclo-synchrotron emission originating from close to the BH. Cyclo-synchrotron emission is polarized, and both linear and circular polarizations have been observed from Sgr A* at several sub-mm wavelengths. The accretion flow was recently

resolved at 230 GHz (Doeleman et al. 2008; Fish et al. 2011). General relativistic (GR) effects were deemed necessary to explain the small size with full width at half maximum (FWHM) of $37\mu\text{as}$. Radio emission is also produced by cyclo-synchrotron at larger distances from the BH. Relativistic frame-dragging is important near the BH, so sub-mm polarized observations and the Compton-scattered X-rays might help to constrain the BH spin. The goal of the present paper is to model the sub-mm in the range of 88 GHz to 857 GHz in order to estimate the accretion flow and black hole parameters.

Sgr A* is a variable source with a variability amplitude routinely reaching 30% in sub-mm. A popular approach is to fit simultaneous observations (e.g. Yuan, Quataert & Narayan 2004; Broderick et al. 2009), in particular, the set from Falcke et al. (1998). However, in such an approach, one would use a single simultaneous set of observations. However, simultaneous observations of fluxes, linear polarization (LP), and circular polarization (CP) fractions at several frequencies are not available. So we consider non-simultaneous statistics of all observations at all frequencies and find the mean values and standard errors of quantities at each frequency.

Numerous accretion flow models have been applied to the Galactic Center: advection-dominated accretion flow (ADAF) (Narayan & Yi 1995), advection-dominated inflow-outflow solution (ADIOS) (Blandford & Begelman 1999), jet-ADAF (Yuan, Markoff & Falcke 2002), jet (Maitra, Markoff & Falcke 2009), and viscous and magnetohydrodynamical (MHD) numerical simulations. The quasi-analytical models are useful because there

roman@astro.umd.edu

¹ <http://astroman.org>

Department of Astronomy, University of Maryland, College Park, MD 20742-2421, USA; Hubble Fellow

² rpenna@cfa.harvard.edu

Harvard-Smithsonian Center for Astrophysics, 60 Garden Street, Cambridge, MA 02138, USA

³ jmckinne@stanford.edu

Department of Physics and Kavli Institute for Particle Astrophysics and Cosmology, Stanford University, Stanford, CA 94305-4060, USA; Chandra Fellow

is little expense in changing parameters. However, they have a large number of free parameters and also incorporate many assumptions that are not justifiable from first principles (Huang et al. 2008, 2009a), which leads to systematic uncertainties in all fits. Numerical simulations require fewer inputs and are useful for more quantitative modeling of the plasma near a rotating BH. General relativistic (GR) MHD (GRMHD) simulations (especially three-dimensional (3D) simulations), which are run over a sufficiently long duration, are still computationally expensive and involve state-of-the-art codes that are still being developed (McKinney & Blandford 2009; Fragile et al. 2009; Noble & Krolik 2009; Moscibrodzka et al. 2009; Penna et al. 2010). Yet, these expensive 3D simulations are required to model the turbulent disk flow, because 2D axisymmetric simulations cannot sustain turbulence as shown by generalizations of Cowling’s anti-dynamo theorem (Hide & Palmer 1982). Given their expense, such 3D GRMHD simulations are limited to a region relatively close to the BH (Dexter et al. 2009; Moscibrodzka et al. 2009), whereas some emission and some Faraday rotation might happen far from the BH. So we analytically extend the modeled region out to $20,000M$, perform radiative transfer, and find the best fit to the data. The extension to large radius allows us to define the electron temperature more consistently (Sharma et al. 2007). We find a posteriori (see Appendix A) that the simulated polarized spectra are not overly sensitive to the details of the analytic extensions of density and temperature, but may depend on the extension of the magnetic field.

The radiation close to the BH has been modeled in Newtonian (Yuan, Quataert & Narayan 2004) and quasi-Newtonian approximations (Goldston, Quataert & Igumenshchev 2005; Chan et al. 2009). It has been modeled in GR assuming unpolarized (Fuerst & Wu 2004; Dexter et al. 2009; Dolence et al. 2009) and polarized (Broderick et al. 2009; Shcherbakov & Huang 2011) light. Fitting the total flux spectrum might not be sufficient to estimate the spin, and naturally one expects polarization to provide extra observational constraints. Spin values from $a_* = 0$ (Broderick et al. 2009) to $a_* = 0.9$ (Moscibrodzka et al. 2009) have been estimated. We neglect Comptonization (Moscibrodzka et al. 2009) and radiation from non-thermal electrons (Mahadevan 1998; Özel, Psaltis & Narayan 2000; Yuan, Quataert & Narayan 2004). Emissivities are calculated in the synchrotron approximation (Legg & Westfold 1968; Sazonov 1969; Pacholczyk 1970; Melrose 1971) with an exact thermal electron distribution. Discrepancies with the exact cyclo-synchrotron emissivities (Leung, Gammie & Noble 2011; Shcherbakov & Huang 2011) are negligible as estimated in § 5. Exact Faraday rotation and conversion expressions are used (Shcherbakov 2008).

We compare simulated spectra to observed ones at many frequencies simultaneously, extending an approach pioneered by Broderick et al. (2009) and Dexter et al. (2009). We compute the average observed spectra, find the deviations of the means, and then compare them to the average simulated spectra. In the search for the best

fit models, we are guided by the value of χ^2/dof , which is the normalized sum of squares of normalized deviations. Yet, we leave the exploration of the statistical meaning of χ^2/dof to future work. We search the space of all parameters: spin a_* , inclination θ , ratio of proton to electron temperatures T_p/T_e (T_p/T_e is reported for radius $6M$), and accretion rate \dot{M} to find the minimum χ^2 models.

We summarize the radio/sub-mm observations of Sgr A* in § 2. Our 3D GRMHD simulations are described in § 3 together with the physically-motivated extension to large radii, and the electron heating prescription. We run simulations for dimensionless spins $a_* = a/M = 0, 0.5, 0.7, 0.9, 0.98$. The GR polarized radiative transfer technique is described in § 5.

The set of observations we consider consists of the spectral energy distribution (SED) within the 88 GHz to 857 GHz frequency range, linear polarization (LP) fractions at 88 GHz, 230 GHz, and 349 GHz, and circular polarization (CP) fractions at 230 GHz and 349 GHz. In § 6 we discuss our results: the best fit models to the observations, the importance of various physical effects in producing the observed CP and LP and electric vector position angle (EVPA), and image size estimates. We produce the simulated images of total and polarized intensities. Discussion in § 7 compares the results to previous estimates, emphasizes the significance of polarization, notes the sources of error, and outlines prospects for future work. In Appendix A we describe a number of convergence tests of our GR polarized radiative transfer code and the radial extension of the dynamical model. Throughout the paper we measure distance and time in the units of BH mass M by setting the speed of light c and gravitational constant G to unity.

2. OBSERVATIONS

Sgr A* is known to be a highly variable source, yet quiescent models of Sgr A* emission are popular and useful. Unlike the drastic variations of X-ray and NIR fluxes (Baganoff et al. 2001; Genzel et al. 2003), sub-mm fluxes do not vary by more than a factor of 2 – 3 (Zhao et al. 2003). We compile the set of observed polarized fluxes at each frequency, then we find the mean spectrum and the errors of the mean fluxes.

Previously, the observed flux spectra were compiled by Yuan, Quataert & Narayan (2004); Broderick et al. (2009). However, both papers summarize a limited set of observations and concentrate on simultaneously observed fluxes. Sub-mm flux data reported in Yuan, Quataert & Narayan (2004) consist of a short set of observations by Falcke et al. (1998) and one set of SMA observations by Zhao et al. (2003). Broderick et al. (2009) adds to these the rest of SMA total flux data (Marrone et al. 2006a,b, 2007, 2008). So 6 out of at least 29 papers on sub-mm observations of Sgr A* were taken into account. We compute an averaged spectrum based on 29 papers reporting sub-mm observations of Sgr A*.

The reported observations vary in covered period from several hours (An et al. 2005) to several years (Zhao et al. 2003; Krichbaum et al. 2006). We know that variations of a factor of 2 may happen within several hours (Yusef-Zadeh et al. 2009), whereas variations by more than a factor of several are never observed in the sub-mm. So, fluxes observed more than a day apart are weakly correlated. The issue of autocorrelation in

TABLE 1
SUMMARY OF SGR A* RADIO/SUB-MM OBSERVATIONS

ν [GHz]	Telescopes	F_ν [Jy]	LP [%]	CP [%]	EVPA [$^\circ$]
8.45	VLA	0.683 ± 0.032 (Serabyn et al. 1997; Falcke et al. 1998; Bower et al. 1999a; An et al. 2005)	...	-0.26 ± 0.06^a (Bower et al. 1999a)	...
14.90	VLBA, VLA	0.871 ± 0.012 (Serabyn et al. 1997; Falcke et al. 1998; Bower et al. 2002; Herrnstein et al. 2004; An et al. 2005; Yusef-Zadeh et al. 2009)	...	-0.62 ± 0.26^a (Bower et al. 2002)	...
22.50	VLBA, VLA	0.979 ± 0.016 (Serabyn et al. 1997; Falcke et al. 1998; Bower et al. 1999b; Herrnstein et al. 2004; An et al. 2005; Lu et al. 2008; Yusef-Zadeh et al. 2007, 2009)	0.20 ± 0.01^a (Bower et al. 1999b; Yusef-Zadeh et al. 2007)
43	GMVA, VLBA, VLA	1.135 ± 0.026 (Falcke et al. 1998; Lo et al. 1998; Bower et al. 1999b; Herrnstein et al. 2004; An et al. 2005; Shen et al. 2005; Krichbaum et al. 2006; Yusef-Zadeh et al. 2007; Lu et al. 2008; Yusef-Zadeh et al. 2009)	0.55 ± 0.22^a (Bower et al. 1999b; Yusef-Zadeh et al. 2007)
88	BIMA, MPIFR, VLBA, VLA, Nobeyama, NMA, CARMA	1.841 ± 0.080 (Falcke et al. 1998; Krichbaum et al. 1998; Bower et al. 1999b; Doeleman et al. 2001; Miyazaki et al. 2004; Shen et al. 2005; Krichbaum et al. 2006; Macquart et al. 2006; Lu et al. 2008; Yusef-Zadeh et al. 2009)	$1.42 \pm 0.5^{a,b}$ (Bower et al. 1999b; Macquart et al. 2006)	...	-4^c (Bower et al. 1999b; Shen et al. 2005; Macquart et al. 2006)
102	OVRO, CSO-JCMT, Nobeyama, NMA, IRAM	1.91 ± 0.15 (Serabyn et al. 1997; Falcke et al. 1998; Miyazaki et al. 2004; Mauerhan et al. 2005; Yusef-Zadeh et al. 2009)
145	Nobeyama, NMA, IRAM, JCMT	2.28 ± 0.26 (Falcke et al. 1998; Aitken et al. 2000; Miyazaki et al. 2004; Yusef-Zadeh et al. 2009)
230	IRAM, JCMT, BIMA, SMA, OVRO	2.64 ± 0.14 (Serabyn et al. 1997; Falcke et al. 1998; Aitken et al. 2000; Bower et al. 2003, 2005; Zhao et al. 2003; Krichbaum et al. 2006; Marrone et al. 2006a, 2007, 2008; Doeleman et al. 2008; Yusef-Zadeh et al. 2009)	7.40 ± 0.66 (Bower et al. 2003, 2005; Marrone et al. 2007, 2008)	-1.2 ± 0.3^a (Munoz et al. (2009, 2011))	111.5 ± 5.3 (Bower et al. 2003, 2005; Marrone et al. 2007, 2008)
349	SMA, CSO, JCMT	3.18 ± 0.12 (Aitken et al. 2000; An et al. 2005; Marrone et al. 2006b, 2007, 2008; Yusef-Zadeh et al. 2009)	6.50 ± 0.61 (Marrone et al. 2006b, 2007)	-1.5 ± 0.3^a (Munoz et al. (2011))	146.9 ± 2.2 (Marrone et al. 2006b, 2007)
674	CSO, SMA	3.29 ± 0.35 (Marrone et al. 2006a, 2008; Yusef-Zadeh et al. 2009)
857	CSO	2.87 ± 0.24 (Serabyn et al. 1997; Marrone et al. 2008; Yusef-Zadeh et al. 2009)

^aThe uncertainty of the mean of these quantities is given by instrumental errors.

^bThe mean LP at 3.5 mm is computed based on lower and upper sidebands in Macquart et al. (2006). The error is based on 0.5% systematic error reported therein.

^cThe mean EVPA at 88 GHz is uncertain due to $\pm 180^\circ$ degeneracy; e.g. the reported EVPA = 80° could as well be interpreted as -100° .

timescales will be addressed in future work. We consider the following averaging technique to sample the distributions of fluxes. First, we define groups of close frequencies, the frequencies in each group being different by no more than several percent from the mean. There are 11 such groups (see Table 1). We exclude papers reporting single frequencies far from the mean of each group. In particular, the 94 GHz and 95 GHz observations of Li et al. (2008); Falcke et al. (1998) and the 112 GHz observations of Bower et al. (2001) are excluded. A mean frequency is ascribed to represent each group. Then, we take all reported observations of each polarization type (total flux, LP and CP fraction, EVPA) for each group and draw the largest sample of fluxes/polarization fractions, taking observations separated by at least 24 hours. When several fluxes are reported over a period of several hours (Yusef-Zadeh et al. 2009), we draw one data point from the very beginning of the observation, unless a flare is reported to occur at that time. Some of the published observations have large error bars. Often such data are produced by observing in sub-mm with large beam size, but light from Sgr A* is blended with dust and other sources. In particular, SMT data (Yusef-Zadeh et al.

2009), early CSO measurements (Serabyn et al. 1997), and early JCMT measurements (Aitken et al. 2000) may have such issues, so we exclude these data from the sample. The interferometric observations, especially with VLBI, help to reduce the error from otherwise unreliable observations, e.g. with BIMA array (Bower et al. 2001). However, some inconsistencies still exist for simultaneous observations at the same frequency with different instruments (Yusef-Zadeh et al. 2009).

After the sample of fluxes, polarization fractions, and EVPAs are found for each frequency group, we compute the mean and the standard error. The summary of results is presented in Table 1. CP fractions of -1.2% at 230 GHz and -1.5% at 349 GHz are based on SMA observations by Munoz et al. (2011) with the reported $\pm 0.3\%$ instrumental error. Note that standard errors in our total flux samples are smaller than the error bars of prior observations (Falcke et al. 1998; Yuan, Quataert & Narayan 2004; Broderick et al. 2009), but still larger compared to contemporary single-observation instrumental errors (Marrone et al. 2007). That is, we do not incorporate instrumental error in our estimates of standard error of the mean fluxes or LP and

EVPA at 230 GHz and 349 GHz (even though the instrumental error of LP at 88 GHz is large). We do not incorporate the source size measurements (Doeleman et al. 2008) in calculating χ^2/dof , but we check that the best bet model is not inconsistent with those observations. Figure 1 shows a compilation of the mean quantities and their Gaussian standard errors. The data are represented by both error bars and the interpolated shaded area. A red dashed curve on the F_ν plot represents the analytic approximation $F_\nu = 0.248\nu^{0.45} \exp(-(\nu/1100)^2)$, where flux is in Jy and frequency is in GHz.

3. THREE-DIMENSIONAL GRMHD SIMULATIONS

Our radiative transfer calculations take the results of simulations of accretion flows onto BHs as input. These simulations are similar to those in Penna et al. (2010). Below, we review the methodology.

3.1. Governing Equations

We simulate radiatively inefficient accretion flows (RIAFs) onto rotating BHs using a three-dimensional fully general relativistic code (see § 3.3). The BH is described by the Kerr metric. We work with Heaviside-Lorentz units. Our five simulations correspond to different choices of the dimensionless BH spin parameter: $a_* = 0, 0.5, 0.7, 0.9$, and 0.98 . The self-gravity of the RIAF is ignored.

The RIAF is a magnetized fluid, so we solve the GRMHD equations of motion (Gammie et al. 2003). Mass conservation gives:

$$\nabla_\mu(\rho u^\mu) = 0, \quad (1)$$

where ρ is the fluid frame rest-mass density, u^μ is the contravariant 4-velocity, and ∇_μ is the covariant derivative. Energy-momentum conservation gives

$$\nabla_\mu T_\nu^\mu = 0, \quad (2)$$

where the stress energy tensor T_ν^μ includes both matter and electromagnetic terms,

$$T_\nu^\mu = (\rho + u_{\text{gas}} + p_{\text{gas}} + b^2)u^\mu u_\nu + (p_{\text{gas}} + b^2/2)\delta_\nu^\mu - b^\mu b_\nu, \quad (3)$$

where u_{gas} is the internal energy density and $p_{\text{gas}} = (\Gamma - 1)u_{\text{gas}}$ is the ideal gas pressure with $\Gamma = 4/3$. Models with $\Gamma = 5/3$ show minor differences compared to models with $\Gamma = 4/3$ (McKinney & Gammie 2004; Mignone & McKinney 2007). The contravariant fluid-frame magnetic 4-field is given by b^μ and is related to the lab-frame 3-field $B^m u$ via $b^\mu = B^\nu h_\nu^\mu / u^t$, where $h_\nu^\mu = u^\mu u_\nu + \delta_\nu^\mu$ is a projection tensor and δ_ν^μ is the Kronecker delta function (Gammie et al. 2003). We often employ \mathbf{b} below, which is the orthonormal magnetic field vector in a comoving locally flat reference frame (Penna et al. 2010). The magnetic energy density (u_b) and magnetic pressure (p_{mag}) are then given by $u_{\text{mag}} = p_{\text{mag}} = b^\mu b_\mu / 2 = b^2 / 2 = \mathbf{b}^2 / 2$. Note that the angular velocity of the gas is $\Omega = u^\phi / u^t$.

Magnetic flux conservation is given by the induction equation

$$\partial_t(\sqrt{-g}B^i) = -\partial_j[\sqrt{-g}(B^i v^j - B^j v^i)], \quad (4)$$

where $v^i = u^i / u^t$, and $g = \text{Det}(g_{\mu\nu})$ is the determinant of the metric. No explicit resistivity or viscosity is included,

but we use a shock-capturing Godunov method that fully conserves energy. So, all dissipation from shocks and numerical diffusivity (e.g. in shear flows or current sheets) is fully captured, as required to study RIAFs.

In Penna et al. (2010), we studied both RIAFs and geometrically thin radiatively efficient disks. For the later case, a cooling term was added to the energy-momentum equation (2) to describe radiative losses and keep the disk thin. The current set of models are all RIAFs, so no cooling term is used. Entropy generated by viscous or resistive dissipation is advected along with the inflow or transported out via convection or in a wind.

3.2. Physical Models

The initial mass distribution is an isentropic equilibrium torus (Chakrabarti 1985a,b; De Villiers, Hawley & Krolik 2003) with pressure $p = K_0 \rho^{4/3}$ for $K_0 = 0.009$. The torus inner edge is at $r_{\text{in}} = 20M$ and the maximum density and pressure are at $R_{\text{max}} = 65M$. We initialize the solution so that $\rho = 1$ at the pressure maximum. As in Chakrabarti (1985a), the angular velocity distribution of the initial torus is a power law, where for the Chakrabarti (1985a) q -parameter we choose $q = 1.65$ (At large radii $\Omega \sim (r/M)^{-q}$). The thickness of the torus at the pressure maximum is then $|h/r| \sim 0.3$, where

$$|h/r| \equiv \frac{\int \int \int |\theta - \pi/2| \rho(r, \theta, \phi) dA_{\theta\phi} dt}{\int \int \int \rho(r, \theta, \phi) dA_{\theta\phi} dt}, \quad (5)$$

where $dA_{\theta\phi} \equiv \sqrt{-g}d\theta d\phi$ is an area element in the $\theta - \phi$ plane, and the integral over dt is a time average over the period when the disk is in a steady state (see §3.6). A tenuous atmosphere fills the space outside the torus. It has the same polytropic equation of state as the torus, $p = K_0 \rho^\Gamma$, with $\Gamma = 4/3$, and an initial rest-mass density of $\rho = 10^{-6}(r/M)^{-3/2}$, corresponding to a Bondi-like atmosphere. The torus is threaded with three loops of weak, poloidal magnetic field: the initial gas-to-magnetic pressure ratio is $\beta = p_{\text{gas,max}}/p_{\text{mag,max}} = 100$, where $p_{\text{gas,max}}$ and $p_{\text{mag,max}}$ are the maximum values of the gas and magnetic pressure in the torus. This approach to normalizing the initial field is used in many other studies (Gammie et al. 2003; McKinney & Gammie 2004; McKinney 2006a; McKinney & Narayan 2007b; Komissarov & McKinney 2007; Penna et al. 2010).

Recent GRMHD simulations of thick disks indicate that the results for the disk (but not the wind-jet, which for us is less important) are roughly independent of the initial field geometry (McKinney & Narayan 2007a,b; Beckwith et al. 2008a, but see also McKinney et al. 2012). The magnetic vector potential we use is given by

$$A_{\phi,N} \propto Q^2 \sin\left(\frac{\log(r/S)}{\lambda_{\text{field}}/(2\pi r)}\right) [1 + 0.02(\text{ranc} - 0.5)], \quad (6)$$

with all other A_μ initially zero. This is the same A_μ as used in Penna et al. (2010). We use $Q = (u_{\text{gas}}/u_{\text{gas,max}} - 0.2)(r/M)^{3/4}$, and set $Q = 0$ if either $r < S$ or $Q < 0$. Here $u_{g,\text{max}}$ is the maximum value of the internal energy density in the torus. We choose $S = 22M$ and

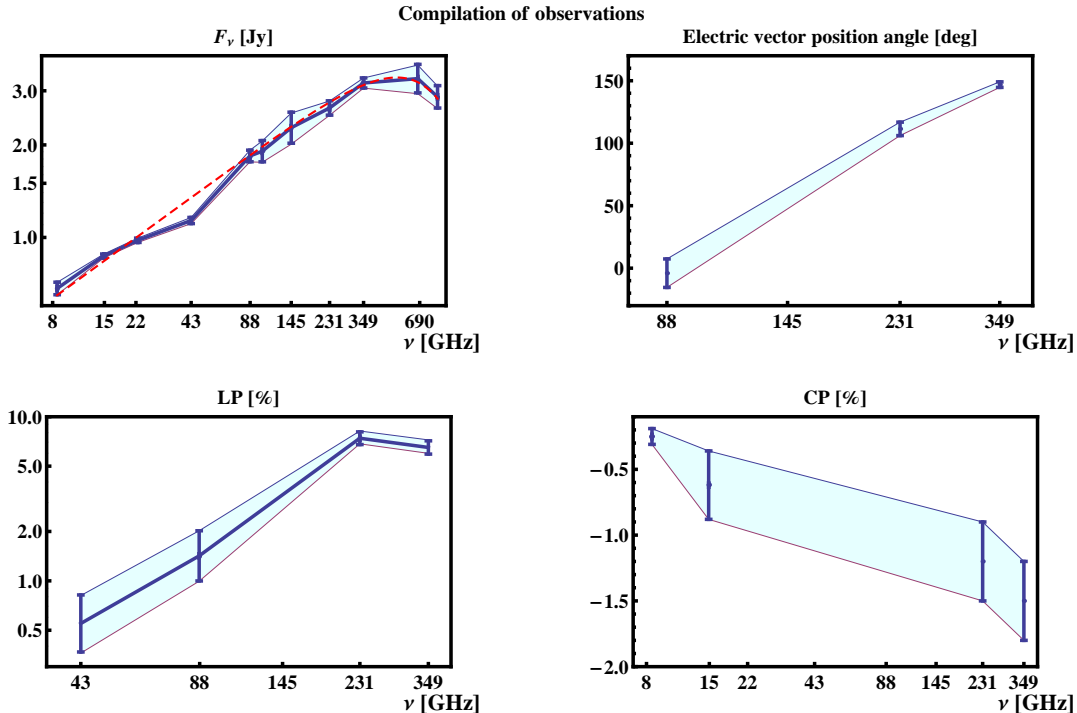


FIG. 1.— Mean observed SEDs of specific flux F_ν , linear polarization (LP) fraction, electric vector position angle (EVPA), and circular polarization (CP) fraction. The error bars show 1σ standard error of the mean. The dashed line on the F_ν plot represents the analytic approximation $F_\nu(\text{Jy}) = 0.248\nu^{0.45} \exp(-(\nu/1100)^2)$ for frequency ν in GHz (not the simulated SED). As noted in Table 1, the error is instrumental for CP at high frequencies 88 and LP at 88 GHz, whereas it is computed from a sample of observed quantities for flux, EVPA at all frequencies, and LP at high frequencies.

$\lambda_{\text{field}}/(2\pi r) = 0.28$, which gives initial poloidal loops that are roughly isotropic such that they have roughly 1:1 aspect ratio in the poloidal plane. The form of the potential in equation (6) ensures that each additional field loop bundle has opposite polarity. Perturbations are introduced to excite the magneto-rotational instability (MRI). The second term on the right-hand-side (RHS) of equation 6 is a random perturbation: `ranc` is a random real number generator for the domain 0 to 1. Random perturbations are introduced in the initial internal energy density in the same way, with an amplitude of 10%. In Penna et al. (2010), it was found that similar simulations with perturbations of 2% and 10% became turbulent at about the same time, the magnetic field energy at that time was negligibly different, and there was no evidence for significant differences in any quantities during inflow equilibrium.

3.3. Numerical Methods

We perform simulations using a fully 3D version of HARM that uses a conservative shock-capturing Godunov scheme (Gammie et al. 2003; Shafee et al. 2008; McKinney 2006b; Noble et al. 2006; Mignone & McKinney 2007; Tchekhovskoy, McKinney & Narayan 2007; McKinney & Blandford 2009). We use horizon-penetrating Kerr-Schild coordinates for the Kerr metric (Gammie et al. 2003; McKinney & Gammie 2004), which avoids any issues with the coordinate singularity in Boyer-Lindquist coordinates. The code uses uniform internal coordinates $(t, x^{(1)}, x^{(2)}, x^{(3)})$ mapped to the physical coordinates (t, r, θ, ϕ) . The radial grid mapping

is

$$r(x^{(1)}) = R_0 + \exp(x^{(1)}), \quad (7)$$

which spans from $R_{\text{in}} = 0.9r_H$ to $R_{\text{out}} = 200M$, where r_H is the radius of the outer event horizon. This just ensures the grid never extends inside the inner horizon, in which case the equations of motion would no longer be hyperbolic. The parameter $R_0 = 0.3M$ controls the resolution near the horizon. For the outer radial boundary of the box, absorbing (outflow, no inflow allowed) boundary conditions are used.

The θ -grid mapping is

$$\theta(x^{(2)}) = \left[Y(2x^{(2)} - 1) + (1 - Y)(2x^{(2)} - 1)^7 + 1 \right] (\pi/2), \quad (8)$$

where $x^{(2)}$ ranges from 0 to 1 (i.e. no cut-out at the poles) and $Y = 0.65$ is chosen to concentrate grid zones toward the equator. Reflecting boundary conditions are used at the polar axes. The ϕ -grid mapping is given by $\phi(x^{(3)}) = 2\pi x^{(3)}$, such that $x^{(3)}$ varies from 0 to 1/2 for a box with $\Delta\phi = \pi$. Periodic boundary conditions are used in the ϕ -direction. Penna et al. (2010) considered various $\Delta\phi$ for thin disks and found little difference in the results. In all of their tests, $\Delta\phi > 7|h/r|$ and we remain above this limit as well. In what follows, spatial integrals are renormalized to refer to the full 2π range in ϕ , even if our computational box size is limited in the ϕ -direction. For the purpose of radiative transfer, we combine two identical regions of size $\Delta\phi = \pi$ preserving the orientation to obtain the span of full 2π .

3.4. Resolution and Spatial Convergence

The resolution of the simulations is $N_r \times N_\theta \times N_\phi = 256 \times 64 \times 32$. This is the fiducial resolution of Penna et al. (2010). Shafee et al. (2008) found this resolution to be sufficient to obtain convergence compared to a similar $512 \times 128 \times 32$ model. In the vertical direction, we have about 7 grid cells per density scale height. Turbulence is powered by the MRI, which is seeded by the vertical component of the magnetic field (Balbus & Hawley 1998). The characteristic length scale of the MRI is the wavelength of the fastest growing mode:

$$\lambda_{\text{MRI}} = 2\pi \frac{v_A^z}{\Omega_0}, \quad (9)$$

where v_A^z is the vertical component of the Alfvén speed. We find that the MRI is well-resolved in the midplane of disk both initially and in the saturated state.

Penna et al. (2010) studied convergence in N_r , N_θ , and N_ϕ and found that models with $N_r = 256$ or $N_r = 512$, $N_\theta = 64$ or $N_\theta = 128$, and $N_\phi = 64$ or $N_\phi = 32$ behaved similar for disks with similar resolution across the disk. Our resolution of the MRI and prior convergence testing by Penna et al. (2010) for similarly-resolved disks justify our choice of grid resolution. It is currently not computationally feasible to perform a similar spin parameter study at much higher resolutions, and future studies will continue to explore whether such simulations are fully converged (Hawley et al. 2011; McKinney et al. 2012).

3.5. Ceiling Constraints

During the simulation, the rest-mass density and internal energy densities can become low beyond the corona, but the code remains accurate and stable for a finite value of b^2/ρ , b^2/u_{gas} , and u_{gas}/ρ for any given resolution. We enforce $b^2/\rho \lesssim 10$, $b^2/u_{\text{gas}} \lesssim 100$, and $u_{\text{gas}}/\rho \lesssim 10$ by injecting a sufficient amount of mass or internal energy into a fixed zero angular momentum observer (ZAMO) frame with 4-velocity $u_\mu = \{-\alpha, 0, 0, 0\}$, where $\alpha = 1/\sqrt{-g^{tt}}$ is the lapse.

We have checked that the ceilings are rarely activated in the regions of interest of the flow. Figure 2 shows the constrained ratios, b^2/ρ , b^2/u_{gas} , and u_{gas}/ρ , as a function of θ at six radii ($r = 4, 6, 8, 10, 12$, and $14M$) for the $a_* = 0$ model. The data has been time-averaged over the steady state period from $t = 14,000M$ to $20,000M$. The ceiling constraints are shown as dashed red lines. The solution stays well away from the ceilings. Thus, the ceilings are sufficiently high.

3.6. Approach to Steady State

We run the simulations from $t = 0M$ to $t = 20,000M$. The accretion rate, the height- and ϕ -averaged plasma β , and other disk parameters, fluctuate turbulently about their mean values. The simulation reaches a quasi-steady state, when the mean parameter value are time-independent. Figure 3 shows the accretion rate and height- and ϕ -averaged $1/\beta$ at the event horizon as a function of time for all five models. We take the period from $t = 14,000M$ to $t = 20,000M$ to define steady state.

As shown in Penna et al. (2010), for disk models like the one considered, the disk outside the innermost stable circular orbit (ISCO) behaves like the α -disk model with $\alpha \sim 0.1$ across disk thicknesses of $h/r \sim 0.05 - 0.4$.

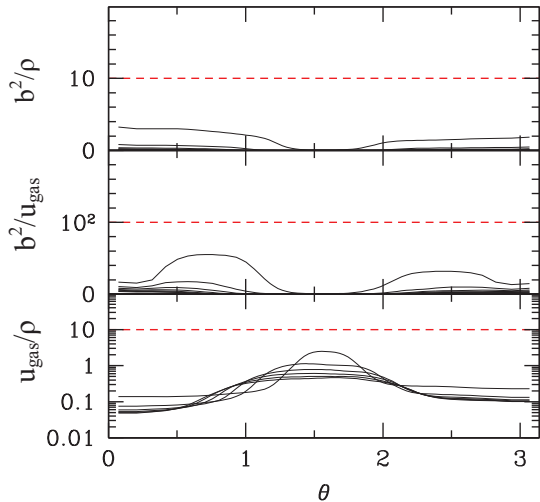


FIG. 2.— Ratios of b^2/ρ , b^2/u_{gas} , and u_{gas}/ρ versus θ . Black curves correspond to different radii in the flow; from top to bottom, $r = 4, 6, 8, 10, 12$, and $14M$. The data is time-averaged over the steady state period of the flow, from $t = 14,000M$ to $20,000M$. Numerical ceilings constrain the solution to lie below the dashed red lines, but we see that the solution does not approach these limits.

This allows one to accurately infer the timescale for reaching “inflow equilibrium,” corresponding to a quasi-steady flow across all quantities, at a given radius. For $h/r \sim 0.3$ by $t \sim 15,000M - 20,000M$ (the simulation runs till $20,000M$, but the initial $5,000M$ are transients not necessarily associated with achieving inflow equilibrium for a simple viscous disk), we use the results in Appendix B of Penna et al. (2010) and find that inflow equilibrium is achieved within a radius of $r \sim 25M - 30M$ for models with $a_* \sim 1$ and $r \sim 35M$ for models with $a \sim 0$. Even for a doubling of the viscous timescale, inflow equilibrium is achieved by $r \sim 20M - 25M$ depending upon the BH spin. This motivates using an analytical extension of the simulation solution for radii beyond $r \sim 25M$ as described later in § 4.1.

3.7. Evolved Disk Structure

Figure 4 shows matter stream lines as vectors and number density n_e as greyscale map. The large scale vortices existing on a single time shot (panel a) almost disappear when averaged over the duration $6,000M$ (panel b) from times $14,000M$ to $20,000M$. The density is highest in the equatorial plane on average, but deviations are present on the instantaneous map. The ISCO does not have any special significance: density and internal energy density increase through ISCO towards the BH horizon.

Figure 5 shows magnetic field lines as vectors and comoving electromagnetic energy density $\propto b^2$ as a greyscale map. The structure of magnetic field at early times remembers the initial multi-loop field geometry (Penna et al. 2010), but switches at late times to a helical magnetic field structure resembling a split-monopole in meridional projection. Such switching of magnetic field structure suggests that the final helix with projected split-monopole is a natural outcome of any vertical flux being dragged into the BH (although the amount of magnetic flux threading the hole and disk may be chosen by initial conditions as described in McKinney et al. 2012).

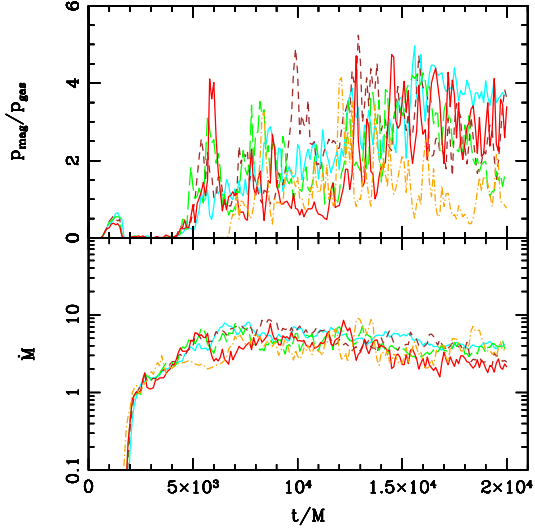


FIG. 3.— Accretion rate and height- and ϕ -averaged $\sigma = p_{\text{mag}}/p_{\text{gas}} = 1/\beta$ versus time at the event horizon for all five models: $a_* = 0$ (solid light cyan), $a_* = 0.5$ (solid dark red), $a_* = 0.7$ (long-dashed green), $a_* = 0.9$ (short-dashed brown), and $a_* = 0.98$ (dot-dashed orange).

The magnetic field structure of a single snapshot (panel a) looks similar to the structure of the linear average between $14,000M$ and $20,000M$ (panel b). The polar region of the flow has the strongest magnetic field. The magnetic field lines on Figure 5 illustrate only the direction of the field's poloidal component. The toroidal magnetic field is stronger above and below the midplane of the disk outside of ISCO. The toroidal field strength is comparable to the poloidal field strength inside the ISCO and near the disk midplane.

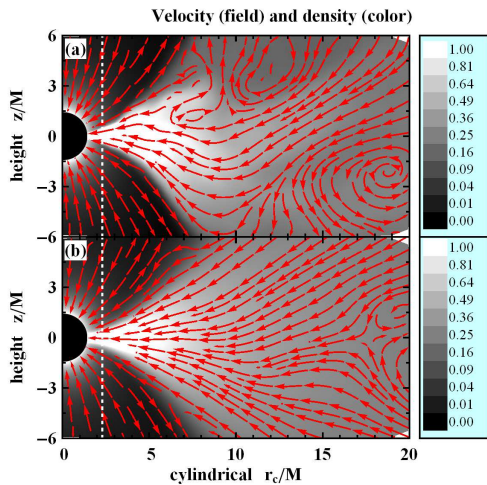


FIG. 4.— Stream lines of velocity (red vectors) and number density n_e (greyscale map) for spin $a_* = 0.9$ at $\phi = 0$ in the meridional plane (r_c as cylindrical radius): single time snapshot at $t = 14,000M$ on the upper (a) panel and time average between $t = 14,000M$ and $t = 20,000M$ on the lower (b) panel. The corresponding calibration bars of n_e are shown on the right. Number density is normalized by its maximum value, and the vectors show the poloidal velocity direction.

4. DYNAMICAL MODEL BASED ON SIMULATIONS

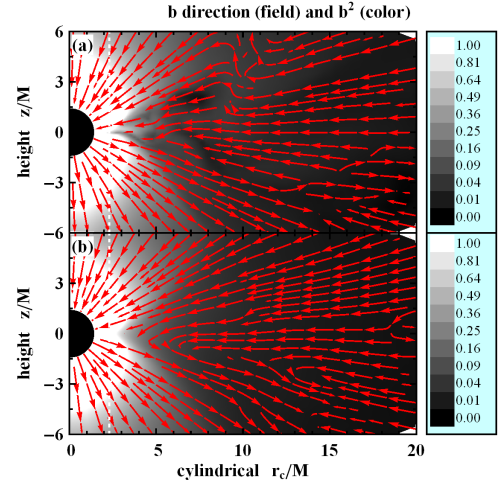


FIG. 5.— Magnetic field lines (red vectors) and comoving electro-magnetic energy density $\propto b^2$ (greyscale map) for spin $a_* = 0.9$ at $\phi = 0$ in the meridional plane (r_c as cylindrical radius): single time snapshot at $t = 14,000M$ on the upper (a) panel and time average between $t = 14,000M$ and $t = 20,000M$ on the lower (b) panel. The corresponding calibration bars of comoving b^2 are shown on the right. Magnetic field energy density is normalized by its maximum value. The magnetic field lines illustrate only the direction of the field's poloidal component.

We now discuss extensions of the numerical simulations, which we need to perform radiative transfer computations. We extend the simulations to large radii and define the electron temperature.

4.1. Extension to Large Radii

The flow is evolved in a quasi-steady state for $6,000M$ from $14,000M$ until $20,000M$, which corresponds to 8 orbits at $r = 25M$. The flow is not sufficiently settled at larger radii. However, outside $25M$, some Faraday rotation and emission might occur. So, we extend the dynamical model to larger radii (i.e. $r > 25M$) in a continuous way and check (see Appendix A) how variations of our large radius prescriptions change the results of radiative transfer. The outer radial boundary of radiative transfer is situated at $r = 20,000M$. The profiles of number density n_e , internal energy density u_{gas} , magnetic field \mathbf{b} , and velocity \mathbf{v} are extended as power-laws until radius $r = 20,000M$. The power-law index for number density β is obtained by matching the known value $n_e = 130\text{cm}^{-3}$ at about $1.5'' \approx 3 \cdot 10^5 M$ (Baganoff et al. 2003) and the average $n_{e,\text{cut}}$ value at $r = 25M$ in the equatorial plane for each model. The value of β may be different for different models. The radial flow velocity v_r is then obtained from the continuity relation in the equatorial plane $n_e v_r r^2 = \text{const}$. The power-law of internal energy density u_{gas} is obtained in a similar way by matching the values $T_e = T_p = 1.5 \cdot 10^7 \text{K}$ and $n_e = 130\text{cm}^{-3}$ at distance $3 \cdot 10^5 M$ (Baganoff et al. 2003; Shcherbakov & Baganoff 2010). The meridional physical velocity is extended as $v_{\hat{\theta}} \propto (r/M)^{-3/2}$ and toroidal velocity as $v_{\hat{\phi}} \propto (r/M)^{-1/2}$ to approximately match the power law between $15M$ and $25M$, where the relationship $v_i \approx u^i \sqrt{g_{ii}}$ is used to connect the 4-velocity components with physical velocity components. All components of comoving magnetic field are extended

as $b_r, b_\theta, b_\phi \propto (r/M)^{-1}$, which appears valid across a diverse set of GRMHD models (McKinney et al. 2012). This power-law slope corresponds roughly to equipartition of magnetic field energy density, since constant fraction magnetic field is $b \propto \sqrt{nT_p} \propto (r/M)^{-1}$ for $n \propto (r/M)^{-1}$. Exploration of various extensions of the magnetic field will be the topic of future studies.

After defining the extension power-laws for quantities in the equatorial plane, we extend the quantities radially at arbitrary θ and ϕ in a continuous way. For example, for density at arbitrary θ and ϕ and at $r > 25M$ we have

$$n_e(r, \theta, \phi) = n_e(25M, \theta, \phi) \left(\frac{r}{25M} \right)^{-\beta}, \quad (10)$$

where $n_e(25M, \theta, \phi)$ is taken from the simulations. We similarly extend other quantities. As shown in Appendix A, small variations in power-law indices of number density and temperature have little influence on radiation intensities and linear/circular polarization fluxes, but variations of magnetic field slope can make a substantial difference.

4.2. Electron Temperature

Neither the proton T_p nor the electron T_e temperature is given directly by the simulations. However, it is crucial to know the electron temperature T_e to determine the emission. Our solution is to split the total internal energy density u_{gas} , given by the simulations and their power-law extension, between the proton energy and the electron energy. The energy balance states

$$\frac{u_{\text{gas}}}{\rho} \equiv \frac{u_{p,g} + u_{e,g}}{\rho} = c_p k_B T_p + c_e k_B T_e, \quad (11)$$

where $c_p = 3/2$ and $c_e \geq 3/2$ are the respective heat capacities, ρ is the rest-mass density, and k_B is Boltzmann's constant. The difference of temperatures $T_p - T_e$ is influenced by three effects: equilibration by Coulomb collisions at large radii, the difference in heating rates f_p and f_e of protons and electrons operating at intermediate radii, and the difference in heat capacities operating close to the BH. Radiative cooling is ignored since, according to Sharma et al. (2007), the radiative efficiency of the flow is negligible for realistic $\dot{M} \lesssim 10^{-7} M_\odot \text{year}^{-1}$. The relevant effects can be summarized by the equation:

$$v_r \frac{d(T_p - T_e)}{dr} = -\nu_c (T_p - T_e) + \left(\frac{1}{c_p} \frac{f_p}{f_p + f_e} - \frac{1}{c'_e} \frac{f_e}{f_p + f_e} \right) v_r \frac{d(u_{\text{gas}}/\rho)}{k_B dr}, \quad (12)$$

where

$$\nu_c = 8.9 \cdot 10^{-11} \left(\frac{T_e}{3 \cdot 10^{10}} \right)^{-3/2} \frac{n_e}{10^7} \quad (13)$$

is the non-relativistic temperature equilibration rate by collisions (Shkarofsky et al. 1966), all quantities being measured in CGS units. We consider protons to always have non-relativistic heat capacity and collisions to always obey the non-relativistic formula. The magnitudes of errors introduced by these simplifications are negligible. The exact expressions for total electron heat capac-

ity and differential heat capacity are approximated as

$$c_e = \frac{u_{e,g}/\rho}{k_B T_e} \approx \frac{3}{2} \frac{0.7 + 2\theta_e}{0.7 + \theta_e}, \quad (14)$$

$$c'_e = \frac{d(u_{e,g}/\rho)}{k_B dT_e} \approx 3 - \frac{0.735}{(0.7 + \theta_e)^2} \quad (15)$$

correspondingly, with the error $< 1.3\%$, where

$$\theta_e = \frac{k_B T_e}{m_e c^2} \quad (16)$$

is the dimensionless electron temperature. It was recently shown (Sharma et al. 2007) that the ratio of heating rates in the non-relativistic regime in a disk can be approximated as

$$\frac{f_e}{f_p} = C \sqrt{\frac{T_e}{T_p}} \quad (17)$$

with coefficient C . This formula is adopted in the relativistic regime as well, since no better prescription is available. Sharma et al. (2007) found the value $C = 0.33$ in simulations, whereas we find $C = 0.36 - 0.42$ for the best fit models (see Table 2 and § 6).

The proton and electron temperatures are determined at each point in the following way. We first take a single snapshot of a simulation with spin a_* and extend the flow quantities to $r = 20,000M$ (see § 4.1). Then we compute azimuthal averages of radial velocity v_r , number density n_e , and u_{gas}/ρ at the equatorial plane, extend them as power laws to $r_{\text{out}} = 3 \cdot 10^5 M$, and solve the equations (11,12) from r_{out} down to the inner grid cell point. Temperatures are set to $T_e = T_p = 1.5 \cdot 10^7$ K at r_{out} (Baganoff et al. 2003; Shcherbakov & Baganoff 2010). On the next step we compare the values of u_{gas}/ρ to the calculated T_e and T_p and determine the functional dependence $T_e = T_e(u_{\text{gas}}/\rho)$ and $T_p = T_p(u_{\text{gas}}/\rho)$. At each point of the simulation (including off the equator), we draw temperatures from this correspondence. That is, GRMHD simulation directly provides u_{gas} and ρ at the equatorial plane, so the function $T_e = T_e(u_{\text{gas}}/\rho)$ gives T_e at each point in space. Typical profiles of proton and electron temperatures are shown on Figure 6. Temperatures stay equal until $r \sim 10^4 M$ due to collisions, despite different heating prescriptions. Within $r = 3 \cdot 10^3 M$ the timescale of collisional equilibration becomes relatively long and electrons become relativistic, thus T_e deviates down from T_p . The electron and proton temperature profiles in the region $r < 20,000M$ are used to conduct the radiative transfer. For a given accretion rate, we find that there exists a unique dependence of the ratio of temperatures T_p/T_e (measured at $r = 6M$ at the equator) upon the heating coefficient C , so that we can use T_p/T_e and C interchangeably.

5. GENERAL RELATIVISTIC POLARIZED RADIATIVE TRANSFER

5.1. Description of Radiative Transfer

Now we convert the dynamical model of the accretion flow into a set of observable quantities using polarized radiative transfer (Broderick et al. 2009; Shcherbakov & Huang 2011). We closely follow Shcherbakov & Huang (2011) for the transfer technique. Similar to Huang et al. (2009a), we define the polarized

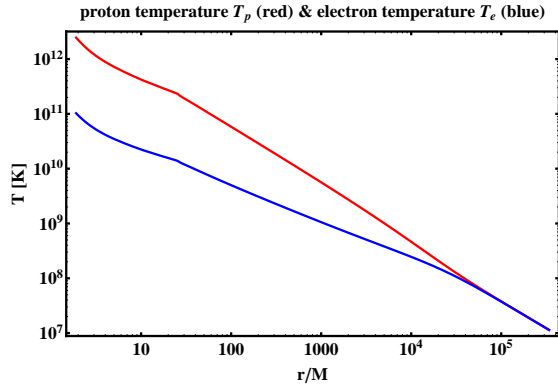


FIG. 6.— Temperatures of protons T_p (upper red line) and electrons T_e (lower blue line) for the dynamical model with spin $a_* = 0.5$ giving the best fit to polarization observations (see Table 2 and § 6).

basis in the picture plane, where one vector points North, another vector points East, and the wavevector points towards the observer. We parallel transport this basis in the direction of the BH and do the radiative transfer along the ray in the opposite direction towards the observer. At each point along the ray we go into the locally-flat comoving frame, calculate the angles between the magnetic field and basis vectors, and compute the Faraday conversion, Faraday rotation, emissivities, and absorptivities.

Radiative transfer involves shooting a uniform grid of $P_N \times P_N$ geodesics from the picture plane down to the black hole. The total polarized fluxes are computed by integration of intensities along each ray backwards to the picture plane. We found that $P_N = 111$ is good enough to compute the spectrum (Dexter et al. 2009 used $P_N = 150$). For radiative transfer we employ all 3D data in each numerical simulation snapshot and, following Moscibrodzka et al. (2009), perform multilinear interpolation in three dimensions for the quantities in between the grid points. We make no approximations in the use of spatial 3D data. We self-consistently take into account the evolution of the numerical simulation as the light geodesics travel around the BH. Since it is too time-consuming to look up simulation data over a long period of time, we only evolve the simulation between $t - \Delta t$ and $t + \Delta t$ to get a spectrum at time $t + 20,000M$. The offset $20,000M$ appears, since the picture plane is located $20,000M$ away from the BH center. The extension to the large radius outside $25M$, however, is not evolved with time. It is taken to be that of a single snapshot at time t . The snapshot at times $t - \Delta t$ and $t + \Delta t$ are taken to represent the numerical simulations at earlier and later times, respectively. We find that $\Delta t = 60M$ is large enough to achieve accurate simulated spectra. The total fluxes are found at regular time intervals within period of quasi-steady accretion from $14,000M$ till $20,000M$, e.g. for $t = 14,000M, 14,300M, \dots, 19,700M, 20,000M$. We compute $N_{\text{periods}} = 21$ spectra over the quasi-steady accretion phase and average them to find the mean simulated spectra. To compute the polarized fluxes we take the integration domain in the picture plane to be a square with a side

$$a[M] = 16 + 2 \left(\frac{600}{\nu[\text{GHz}]} \right)^{1.5} \quad (18)$$

in the units of $r_g \equiv M$, where frequency ν is in GHz. This square is centered at the BH. The size based on Equation (18) is larger than the photon orbit visible diameter $d_{\text{ph}} \approx 10.4M$ and follows the intrinsic size dependence on frequency (Shen et al. 2005; Doeleman et al. 2008) at low frequencies. An important radiative transfer parameter is the distance from the BH, where intensity integration starts. The dependence of synchrotron emissivity on temperature and magnetic field strength is so strong that it overwhelms the sole effect of gravitational redshift close to the BH. We obtain accurate results in the sub-mm for computation out from $r_{\text{min}} = 1.01r_H$, where $r_H = M(1 + \sqrt{1 - a_*^2})$ is the horizon radius. To quantify the needed accuracy of computations, we define a quantity χ_H^2/dof in Appendix A. We conduct multiple tests of radiative transfer convergence for best fit models at each spin. In Appendix A, we justify the chosen values of radiative transfer parameters P_N , Δt , N_{periods} , r_{min} , etc.

Our calculation of plasma response is different from Shcherbakov & Huang (2011). They offered a way to find exact emissivities, absorptivities, Faraday rotation, and conversion coefficients for thermal and other isotropic particle distributions. Here, for simplicity, we employ fitting formulas for Faraday rotation and Faraday conversion and synchrotron approximation for emissivities for a thermal plasma. We define

$$X = \frac{2}{3} \frac{\nu}{\nu_B \gamma^2 \sin \theta_B}, \quad (19)$$

where θ_B is $\mathbf{k}\text{-}\mathbf{b}$ angle, γ is electron gamma factor, and $\nu_B = eb/(2\pi m_e c)$ is the cyclotron frequency. Then following Legg & Westfold (1968); Melrose (1971), we write down emissivities in the I , Q , and V modes as

$$\begin{aligned} \varepsilon_I &= \frac{\sqrt{3}}{2} \frac{e^2}{c} \nu_B \sin \theta_B \int_1^{+\infty} d\gamma N(\gamma) X \int_X^{+\infty} dz K_{5/3}(z), \\ \varepsilon_Q &= \frac{\sqrt{3}}{2} \frac{e^2}{c} \nu_B \sin \theta_B \int_1^{+\infty} d\gamma N(\gamma) X K_{2/3}(X), \\ \varepsilon_V &= \frac{2}{\sqrt{3}} \frac{e^2}{c} \nu_B \cos \theta_B \int_1^{+\infty} d\gamma \frac{N(\gamma)}{\gamma} \times \\ &\quad \times \left[X K_{1/3}(X) + \int_X^{+\infty} dz K_{1/3}(z) \right]. \end{aligned} \quad (20)$$

Here $K_z(x)$ is the Bessel function of the 2nd kind of order z . We employed IEEE/IAU definitions of Stokes Q , U , and V (Hamaker & Bregman 1996), and we define counter-clockwise rotation of the electric field as seen by the observer as corresponding to positive $V > 0$ – as also chosen in Shcherbakov & Huang (2011). So, the sign of the V emissivity (Eq. 20) is opposite to the sign in Rybicki & Lightman (1967). A variation of emissivity formulas (19,20) exists: Sazonov (1969); Pacholczyk (1970) define $X = 2\nu/(3\nu_B(\gamma - 1)^2 \sin \theta_B)$, integrating over particle energy instead of γ . This approximation appears to give significantly larger errors at low particle energies.

Next, one needs to identify the accurate thermal particle distribution $N(\gamma)$. Various $N(\gamma)$ correspond to various synchrotron approximations. The ultrarelativistic thermal approximation (Pacholczyk 1970; Huang et al.

2009a) has the simplest distribution $N(\gamma) = \exp(-(\gamma - 1)/\theta_e)(\gamma - 1)^2/2/\theta_e^3$. However, the exact thermal distribution of particles

$$N(\gamma) = \gamma \sqrt{\gamma^2 - 1} \frac{\exp(-\gamma/\theta_e)}{\theta_e K_2(\theta_e^{-1})} \quad (21)$$

allows for more precise computation of radiation. Synchrotron emissivities based on the equations (19,20) with the exact thermal distribution (21) agree with the exact cyclo-synchrotron emissivities ε_I , ε_Q , and ε_V (Leung, Gammie & Noble 2011; Shcherbakov & Huang 2011) to within 2% for typical dynamical models and frequencies > 100 GHz. Emissivities integrated over the ultrarelativistic thermal distribution typically have $\sim 10\%$ error.

Thermal absorptivities are found from emissivities (Eq. 20) via Kirchhoff's law

$$\alpha_{I,Q,V} = \varepsilon_{I,Q,V}/B_\nu, \quad (22)$$

where $B_\nu = 2k_B T_e \nu^2/c^2$ is the source function for low photon energies ($h\nu \ll k_B T_e$). Faraday rotation ρ_V and Faraday conversion ρ_Q coefficients are taken from Shcherbakov (2008):

$$\begin{aligned} \rho_V &= g(Z) \frac{2n_e e^2 \nu_B K_0(\theta_e^{-1})}{m_e c \nu^2 K_2(\theta_e^{-1})} \cos \theta, \quad (23) \\ \rho_Q &= f(Z) \frac{n_e e^2 \nu_B^2}{m_e c \nu^3} \left[\frac{K_1(\theta_e^{-1})}{K_2(\theta_e^{-1})} + 6\theta_e \right] \sin^2 \theta. \end{aligned}$$

Here

$$Z = \theta_e \sqrt{\sqrt{2} \sin \theta \left(10^3 \frac{\nu_B}{\nu} \right)} \quad (24)$$

and

$$\begin{aligned} g(Z) &= 1 - 0.11 \ln(1 + 0.035Z), \\ f(Z) &= 2.011 \exp\left(-\frac{Z^{1.035}}{4.7}\right) - \\ &\quad - \cos\left(\frac{Z}{2}\right) \exp\left(-\frac{Z^{1.2}}{2.73}\right) - 0.011 \exp\left(-\frac{Z}{47.2}\right) \end{aligned} \quad (25)$$

are the fitting formulas for deviations of ρ_V and ρ_Q from analytic results for finite ratios of ν_B/ν . The deviation of $f(Z)$ from 1 is significant for the set of observed frequencies ν , temperatures θ_e , and magnetic fields found in the typical models of Sgr A*. These formulas constitute a good fit to the exact result for the typical parameters of the dynamical model (Shcherbakov 2008).

Polarized radiative transfer can take much longer to perform compared to non-polarized radiative transfer when using an explicit integration scheme to evolve the Stokes occupation numbers N_Q , N_U , and N_V . Large Faraday rotation measure and Faraday conversion measure lead to oscillations between occupation numbers. One of the solutions is to use an implicit integration scheme, while another solution is to perform a substitution of variables. In the simple case of Faraday rotation leading to interchange of N_Q and N_U , our choice of variables is the amplitude of oscillations and the phase. Thus, the cylindrical polarized coordinates arise as fol-

lows:

$$\begin{aligned} N_Q &= N_{QU} \cos \phi, \\ N_U &= N_{QU} \sin \phi. \end{aligned} \quad (26)$$

Then, the amplitude N_{QU} slowly changes along the ray and the angle ϕ changes linearly, and this translates into a speed improvement. In the presence of substantial Faraday conversion, the polarization vector precesses along some axis on a Poincaré sphere, adding an interchange of circularly and linearly polarized light. So, polar polarized coordinates are more suitable in this case:

$$\begin{aligned} N_Q &= N_{\text{pol}} \cos \phi \sin \psi, \\ N_U &= N_{\text{pol}} \sin \phi \sin \psi, \\ N_V &= N_{\text{pol}} \cos \psi, \end{aligned} \quad (27)$$

where N_{pol} is the total polarized intensity, ϕ angle changes are mainly due to Faraday rotation, and ψ angle changes are mainly due to Faraday conversion. The application of this technique speeds up the code enormously at low frequencies of $\nu < 100$ GHz.

5.2. Search for the Best Fits

We define χ^2/dof quantities to discriminate between models. We define χ_F^2 for fitting total fluxes as

$$\chi_F^2 = \sum_{i=1}^7 \frac{(F_{i,\text{sim}} - F_{i,\text{obs}})^2}{\sigma(F)^2}, \quad (28)$$

for the set of 7 frequencies $\nu = 88, 102, 145, 230, 349, 680,$ and 857 GHz, where $\sigma(F)$ are the errors of the means. We incorporate LP fractions at 88, 230, and 349 GHz and CP fractions at 230 and 349 GHz to obtain

$$\begin{aligned} \chi^2 &= \chi_F^2 + \sum_{i=1}^3 \frac{(\text{LP}_{i,\text{sim}} - \text{LP}_{i,\text{obs}})^2}{\sigma(\text{LP})^2} \\ &\quad + \sum_{i=1}^2 \frac{(\text{CP}_{i,\text{sim}} - \text{CP}_{i,\text{obs}})^2}{\sigma(\text{CP})^2}. \end{aligned} \quad (29)$$

Then we define dof (as degrees of freedom) to be $\text{dof}_F = 7 - 3 = 4$ for flux fitting and $\text{dof} = 12 - 3 = 9$ for fitting all polarized data. The quantity χ^2/dof would be drawn from χ^2 statistics if σ -s were the true observational errors and if the observed fluxes were drawn from a Gaussian distribution. However, for the purpose of the present work, we only employ χ^2/dof as a measure of fitting the data. That is, lower χ^2/dof indicates better agreement with the data. We do not attempt to ascribe any statistical meaning to the quantity χ^2/dof .

We explore models with 4 parameters: spin a_* , inclination angle θ , accretion rate \dot{M} , and the ratio of proton to electron temperature T_p/T_e (T_p/T_e is reported for radius $r = 6M$). For the radiative transfer calculations, the density from the simulations is scaled to give the desired accretion rate.

6. RESULTS

In previous sections, we described our compiled observations, GRMHD numerical simulations of the flow structure, our method for obtaining the electron temperature, and our method for polarized radiative transfer. In

TABLE 2
PROPERTIES OF THE BEST FIT MODELS WITH DIFFERENT SPINS.

Model	Inclination angle θ , deg	Spin position angle PA, deg	Heating constant C	Ratio T_p/T_e at $6M$	Electron temperature T_e at $6M$, K	Accretion rate \dot{M} , $M_\odot \text{yr}^{-1}$
spin $a_* = 0$	42.0	171.0	0.42107	15.98	$3.343 \cdot 10^{10}$	$7.005 \cdot 10^{-8}$
spin $a_* = 0.5$	74.5	115.3	0.37012	20.14	$3.087 \cdot 10^{10}$	$4.594 \cdot 10^{-8}$
spin $a_* = 0.7$	64.5	84.7	0.37239	20.16	$3.415 \cdot 10^{10}$	$2.694 \cdot 10^{-8}$
spin $a_* = 0.9$	53.5	123.4	0.39849	18.16	$4.055 \cdot 10^{10}$	$1.402 \cdot 10^{-8}$
spin $a_* = 0.98$	57.2	120.3	0.41343	17.00	$4.190 \cdot 10^{10}$	$1.553 \cdot 10^{-8}$
spin $a_* = 0.5$ short period 1	70.0	79.3	0.38934	18.50	$3.334 \cdot 10^{10}$	$3.513 \cdot 10^{-8}$
spin $a_* = 0.5$ short period 2	72.8	113.1	0.40507	17.31	$3.541 \cdot 10^{10}$	$3.452 \cdot 10^{-8}$
spin $a_* = 0.5$ short period 3	73.4	57.4	0.37302	19.87	$3.125 \cdot 10^{10}$	$3.897 \cdot 10^{-8}$
spin $a_* = 0.5$ short period 4	74.4	115.4	0.36147	20.95	$2.978 \cdot 10^{10}$	$4.508 \cdot 10^{-8}$
spin $a_* = 0.5$ short period 5	71.9	95.7	0.37420	19.79	$3.137 \cdot 10^{10}$	$5.334 \cdot 10^{-8}$
spin $a_* = 0.5$ short period 6	76.4	116.7	0.38853	18.59	$3.320 \cdot 10^{10}$	$6.080 \cdot 10^{-8}$
spin $a_* = 0$ fast light	41.4	187.5	0.41929	16.09	$3.322 \cdot 10^{10}$	$7.044 \cdot 10^{-8}$
spin $a_* = 0.5$ fast light	72.7	105.9	0.39804	17.83	$3.447 \cdot 10^{10}$	$3.957 \cdot 10^{-8}$
spin $a_* = 0.7$ fast light	59.4	131.8	0.35708	21.62	$3.204 \cdot 10^{10}$	$2.966 \cdot 10^{-8}$
spin $a_* = 0.9$ fast light	53.3	123.3	0.40215	17.86	$4.116 \cdot 10^{10}$	$1.340 \cdot 10^{-8}$
spin $a_* = 0.98$ fast light	57.7	119.6	0.41720	16.73	$4.246 \cdot 10^{10}$	$1.515 \cdot 10^{-8}$

NOTE. — Mean values are shown for ratio T_p/T_e , electron temperature T_e , and the accretion rate \dot{M} . These are the simple means over all simulation snapshots, which were employed for radiative transfer in a particular model. The values of χ^2/dof ranges from 2–5 across all models.

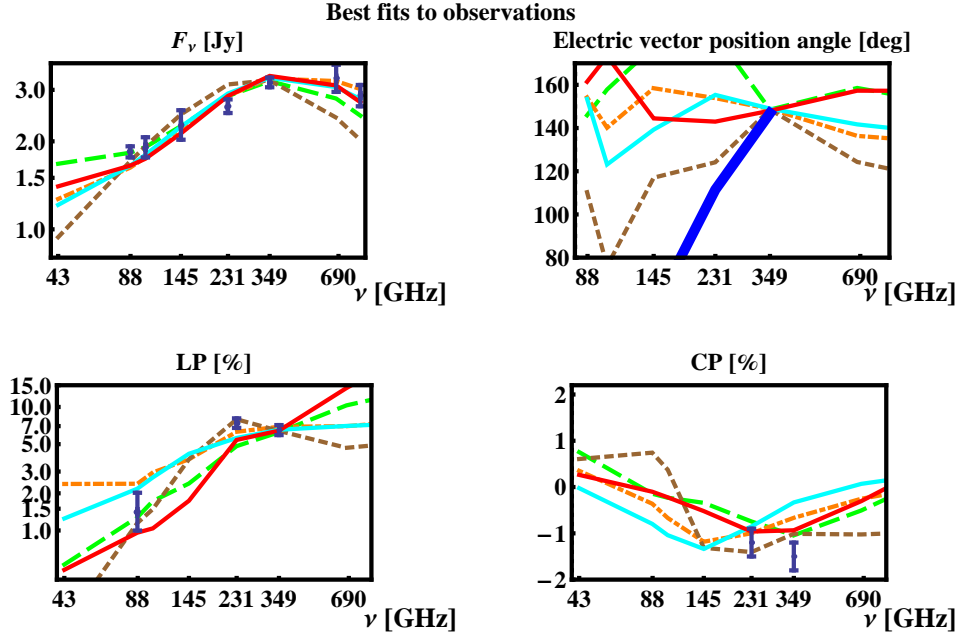


FIG. 7.— Fits to the observed fluxes, LP and CP fractions by best models for each spin. The inclination angle θ , accretion rate \dot{M} , ratio of temperatures T_p/T_e were adjusted for each spin to minimize χ^2/dof . Fits to total flux F_ν are in the upper left panel, LP fraction in the lower left, and CP fraction in the lower right. Shown are the best fit models with spin $a_* = 0$ (short-dashed brown), spin $a_* = 0.5$ (solid dark red), spin $a_* = 0.7$ (long-dashed green), spin $a_* = 0.9$ (solid light cyan), and spin $a_* = 0.98$ (dot-dashed orange). The upper right panel shows the dependence of EVPA on frequency for the best models. Note, that EVPAs are not included into our fitting procedure. The thick blue curve represents observations. Simulated EVPA curves are arbitrarily shifted to approximate EVPA at 349 GHz. The addition of an external (to the emitting region) Faraday rotation screen helps to fit EVPA(349 GHz) – EVPA(230 GHz).

this section, we discuss our results for accretion flow and BH parameters, as guided by a minimization of χ^2/dof

for our model applied to the observations.

Figure 7 shows best fits to observations by models with five different spins. Inclination angle θ , accretion rate \dot{M} , and heating coefficient C were adjusted to reach the lowest χ^2/dof . Fits to fluxes F_ν (upper left) are not substantially different, although models with higher spins fit better at high frequencies. Larger deviations can be seen on LP (lower left) and CP (lower right) plots. Models with high spins require lower accretion rate (i.e. density) to fit the flux spectrum. As a consequence, they are not subject to Faraday depolarization, which leads to a decrease of LP at low ν , and the models end up having larger linear polarization fractions at 88 GHz. Not all models reproduce the observed decrease of mean LP fraction between 230 GHz and 349 GHz groups. The discrepancies in fitting the CP fraction are also large: all the lowest χ^2 models give $|\text{CP}| < 1.5\%$ at 349 GHz. The best bet model with spin $a_* = 0$ reproduces LP and CP fractions well, but fails in fitting the total flux. Most solutions predict the wrong sign of the EVPA(349 GHz) – EVPA(230 GHz) difference, which could be fixed with stronger magnetic field (e.g. as seen in models by McKinney et al. 2012) to yield stronger Faraday rotation. In sum, crude agreement of simulated polarized spectra to the observed ones was achieved, but the improved dynamical models may be needed for better fits.

We now isolate the physical effects responsible for the observed polarized quantities for our best bet model with spin $a_* = 0.5$ that has the lowest χ^2/dof (see subsection 6.1).

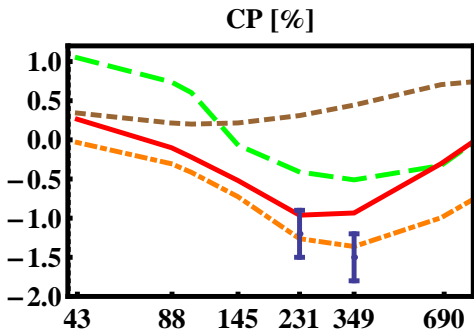


FIG. 8.— Contributions of different effects to the CP fraction as a function of frequency for our best bet model with BH spin $a_* = 0.5$. Shown are observations (blue error bars), the best bet model (solid red line), the same dynamical model computed with zero V emissivity ($\varepsilon_V = 0$) in radiative transfer so that CP is produced by Faraday conversion (dot-dashed orange), the same model with zero Faraday conversion ($\rho_Q = 0$) (short-dashed brown), and the same model with zero Faraday rotation ($\rho_V = 0$) (long-dashed green). Emissivity in circular V mode contributes little to the observed CP, which is mainly due to Faraday conversion.

There are several radiative transfer effects that contribute similarly to the polarized fluxes. Let us consider the production of circular polarization in the flow. Figure 8 shows the consequence of switching off each physical effect for our best bet model with spin $a_* = 0.5$. The solid red curve is the result with all physics on. The dot-dashed orange line below is for zero circular emissivity having $\varepsilon_V = 0$. The brown dashed line corre-

sponds to zero Faraday conversion ($\rho_Q = 0$). Switching off ε_V emissivity leads to a minor correction, whereas setting Faraday conversion to zero results in CP of the opposite sign with several times smaller absolute value. Most of the CP in this model is produced by Faraday conversion. It would be incorrect, however, to think that the simple linear to circular conversion explains the observed CP. The dashed green line in Figure 8 shows the CP fraction, when Faraday rotation is switched off ($\rho_V = 0$). The effect of Faraday rotation is insignificant at $\nu > 350$ GHz, but the rotation of the plane of linear polarization simultaneous with conversion between linear and circular polarizations produces a unique effect at lower ν . This is the so-called “rotation-induced conversion” (Homan et al. 2009). Sign oscillations of V with frequency do not happen when the Faraday rotation is on, but they do happen when $\rho_V = 0$. For the best fit model it is the rotation-induced Faraday rotation, which is responsible for the most of circularly polarized light.

In Figure 9 we illustrate the influence of Faraday rotation on LP fraction (left panel) and EVPA (right panel). The solid curves are produced with all physics on for our best bet model with spin $a_* = 0.5$. The green dashed lines are computed when switching off Faraday rotation ($\rho_V = 0$). The Faraday rotation is small at high frequencies and LP curves look similar at $\nu > 200$ GHz. As the rotation of polarization plane is much stronger at low ν , a significant phase shift accumulates between different rays at the low end of the spectrum and cancellations of LP become strong at $\nu < 150$ GHz. This illustrates the effect of Faraday depolarization (Bower et al. 1999a). In the absence of Faraday rotation, the dependence of EVPA on frequency is not constant: the variations of intrinsic emitted EVPA are significant. Thus, the change of EVPA with ν should not always be ascribed to the effect of Faraday rotation. The positive observed slope of EVPA with ν at high ν , acquired due to negative Faraday rotation measure ($RM < 0$), is comparable to the slope of intrinsic emitted EVPA.

There is an alternate way to test dynamical models against observations. The intrinsic image size was recently measured (Doeleman et al. 2008) with the VLBI technique. The measured correlated flux at 230 GHz was $F_{\text{corr}} \approx 0.35$ Jy at 3.5 G λ SMT-JCMT baseline. Similar values of correlated flux were observed later by the same group (Fish et al. 2011). We plot this correlated flux with 3σ error bar in Figure 10 and compare it to simulated correlated fluxes. To simulate the correlated flux we follow Fish et al. (2009) and employ a Gaussian interstellar scattering ellipse with half-widths at half-maximum $7.0 \times 3.8G\lambda$ with position angle 170° East of North. The correlated fluxes for the best fit models with spin $a_* = 0.5$ (darker red lines) and $a_* = 0.98$ (lighter orange lines) are shown. We vary the position angle (PA) of the BH spin axis, and plot correlated flux curves with the largest (upper solid lines) and the smallest (lower dashed lines) correlated flux at $3.5G\lambda$. Since we do not fit EVPA directly, models with different PA have the same χ^2/dof . The size in our best bet model with spin $a_* = 0.5$ is consistent with observations, whereas the best fit model with spin $a_* = 0.98$ has larger correlated flux, so that the size of the shadow is slightly under-predicted. The simulated source size is in crude agreement to the observed one.

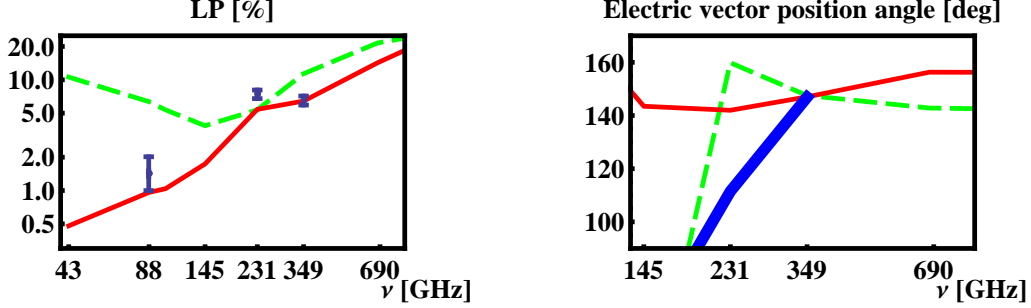


FIG. 9.— Contributions of different effects to the LP fraction (on the left) and EVPA (on the right) as functions of frequency for the best fit model with spin $a_* = 0.5$. Shown are observations (blue error bars and thick blue line), the best fit model (solid red line), and the same dynamical model computed with zero Faraday rotation ($\rho_V = 0$) in radiative transfer (long-dashed green). Beam depolarization is weak: if Faraday rotation is absent, then LP stays high at low frequencies. Even when the Faraday rotation is set to zero, the EVPA depends on frequency due to varying intrinsic emission EVPA. Faraday rotation in the best fit model is too weak to reproduce EVPA observations, so stronger magnetic fields or more magnetic flux near the black hole than in the simulations may be required.

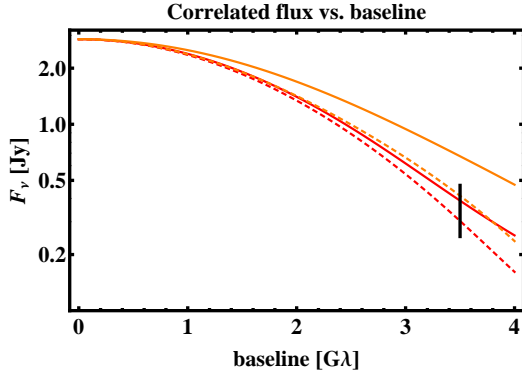


FIG. 10.— Correlated flux as a function of baseline at 230 GHz normalized to the averaged observed flux at 2.82 Jy for the best fit models with spin $a_* = 0.5$ (darker red lines) and $a_* = 0.98$ (lighter orange lines). The upper solid lines show the smallest size (largest correlated flux) over all position angles of BH spin axis, and the lower dashed lines show the largest size (smallest correlated flux) over all position angles. An observational results presented in Doeleman et al. (2008) with 3σ error bars at baseline 3.5 Gλ is depicted as a vertical black bar for comparison. The size in our best fit model with spin $a_* = 0.5$ is consistent with observations, whereas the best fit model with spin $a_* = 0.98$ has larger correlated flux, so that the size of the shadow is slightly under-predicted.

Table 2 summarizes the properties of several best fit models. Rows 1 – 5 show the model parameters for best fits with spins from $a_* = 0$ to $a_* = 0.98$. The simulated spectra are computed every $300M$ from $t = 14,000M$ till $t = 20,000M$ for $\Delta t = 60M$. Then $N_{\text{period}} = 21$ spectra are averaged to compare to observations. The rows 6 – 11 show the model parameters for models with spin $a_* = 0.5$ for spectra averaged over shorter periods. That is, $N_{\text{period}} = 21$ spectra are computed from $t = 14,000M$ till $t = 15,000M$ for the 1-st short period, while the second short period covers the time interval from $t = 15,000M$ till $t = 16,000M$, etc. When comparing the best fit models with spin $a_* = 0.5$ computed over different simulation periods, we find variations in inclination angle $\Delta\theta = 3^\circ$ from the mean, the electron temperature $\Delta T_e/T_e = 10\%$, and the accretion rate $\Delta\dot{M}/\dot{M} = 30\%$. The spin position angle varies by as much as $\Delta\text{PA} = 30^\circ$.

The last 5 rows in Table 2 show the model parameters for best fits within the “fast light” approximation. In this approximation, simulated spectra are computed

over single frozen snapshots, e.g. for $\Delta t = 0$. When the fast light approximation is used instead of the correct simultaneous evolution of photon field and MHD, the models with spins $a_* = 0; 0.9; 0.98$ produce almost identical best fits with variations $\Delta\theta < 0.6^\circ$, $\Delta T_e/T_e < 1.5\%$, and $\Delta\dot{M}/\dot{M} < 5\%$. However, the models with $a_* = 0.5; 0.7$ settle to different χ^2/dof minima with larger changes in quantities: $\Delta\theta = 5^\circ$, $\Delta T_e/T_e = 10\%$, $\Delta\dot{M}/\dot{M} = 10\%$. These variations are still smaller than variations between models with different spins. Switching to the fast light approximation results in significant changes $\Delta\chi^2/\text{dof} \sim 1$ between the best fit models for the same spins, which emphasizes the importance of precise radiation transfer calculations.

6.1. Model Parameters

We now discuss the estimated parameters obtained for the best fit models. The best fit model with spin $a_* = 0.5$ has inclination angle $\theta = 74.5^\circ$, mean accretion rate $\dot{M} = 4.6 \times 10^{-8} M_\odot \text{year}^{-1}$, ratio of temperatures $T_p/T_e = 20.1$ at $r = 6M$, which gives $T_e = 3.1 \cdot 10^{10}$ K at $r = 6M$ in the equatorial plane. The best fit models with other spins give the inclination angles: $\theta = 42^\circ, 64.5^\circ, 53.5^\circ, 57.2^\circ$ at $a_* = 0; 0.7; 0.9; 0.98$, respectively. Thus, the inclination angle for the 5 models lies within $\theta = 42^\circ - 75^\circ$. Our modeling favors neither edge-on nor face-on orientations. The electron temperature T_e at $r = 6M$ is surprisingly uniform over a set of best fit models. All 5 best fit models with spins from $a_* = 0$ to $a_* = 0.98$ presented in Table 2 have electron temperature within the tight range

$$T_e = (3.0 - 4.2) \times 10^{10} \text{K}. \quad (30)$$

The accretion rate depends strongly on spin. The model with spin $a_* = 0$ has an accretion rate $\dot{M} = 7.0 \times 10^8 M_\odot \text{year}^{-1}$, which is 5 times larger than the accretion rate $\dot{M} = 1.4 \times 10^8 M_\odot \text{year}^{-1}$ for the model with spin $a_* = 0.9$. Higher spin values give lower accretion rates. A natural outcome of fitting polarized spectrum is the PA of the BH spin axis. Similar to Huang et al. (2009a), we rely on the observed intrinsic EVPA $\approx 111.5^\circ$ at 230 GHz and EVPA $\approx 146.9^\circ$ at 349 GHz (see § 2). For the model to fit the difference in EVPA, we add a Faraday rotation

screen far from the BH with constant rotation measure (RM). Then we compute the required RM and the intrinsic PA to fit the simulated EVPAs at 230 and 349 GHz. The best bet model with $a_* = 0.5$ gives $\text{PA} = 115.3^\circ$ East of North, whereas the next best fit model with spin $a_* = 0.98$ requires $\text{PA} = 120.3^\circ$. However, PA is different by 90° between the models with spin $a_* = 0$ and $a_* = 0.7$, which indicates that PA can lie within a wide range. In sum, some parameters, such as T_e , are estimated to be in narrow ranges, while only order of magnitude estimates are available for other parameters, such as \dot{M} .

With the estimated orientation of the BH spin axis, we can plot an image of average radiation intensity from near the event horizon. Figure 11 shows images of total intensity I_ν for the best bet model with spin $a_* = 0.5$ (upper left panel), the best fit for spin $a_* = 0.98$ (lower left panel), and LP intensity and CP intensity plots for the best bet model with $a_* = 0.5$ (upper right and lower right panels, correspondingly). The LP average intensity plot was made by averaging U and Q intensities separately and then finding the total LP fraction and EVPA. Blue (predominant) color on the CP plot depicts the regions with negative CP intensity and red (scarce) color depicts the regions with positive CP intensity. The total V flux from this solution is negative ($V < 0$). The streamlines on the LP plot are aligned with EVPA direction at each point. The spin axis is rotated by $\text{PA} = 115.3^\circ$ East of North for the best bet model with spin $a_* = 0.5$ and by $\text{PA} = 120.3^\circ$ for the best fit model with spin $a_* = 0.98$. The spin axis is inclined at θ to the line of sight, so that the either right (West) or left (East) portions of the flow are closer to the observer. The color schemes on all plots are nonlinear with corresponding calibration bars plotted on the sides. The numbers at the top of calibration bars denote normalizations.

7. DISCUSSION AND CONCLUSIONS

Let us compare our results with estimates of Sgr A* accretion flow and BH parameters made by other researchers.

Two separate searches for spin based on GRMHD numerical simulations have been reported so far: Moscibrodzka et al. (2009) and Dexter et al. (2010). Moscibrodzka et al. (2009) considered the set of spins from $a_* = 0.5$ to $a_* = 0.98$ for 2D GRMHD simulations, then fitted the X-Ray flux, the 230 GHz flux, and the flux slope at 230 GHz. They found at least one model for each spin is crudely consistent with the observations (see their table 3), and their best bet model has $a_* = 0.9$. Dexter et al. (2010) focused on a set of 3D GRMHD, then fitted the 230 GHz flux and size estimates, and they provided a table of spin probabilities with $a_* = 0.9$ having the highest $P(a)$. When we fitted the spectrum and LP/CP fractions, the model with $a_* = 0.5$ has the lowest χ^2/dof . As for these two groups, we are also unable to provide a statistically significant constraint on a_* . Other spin estimates have been based on analytic models. Broderick et al. (2009, 2010) favor $a_* = 0$ solutions, while Huang et al. (2009b) favor $a_* < 0.9$ (although they do not explore their full model parameter space).

Another poorly constrained quantity is the mass accretion rate. Our estimate $\dot{M}_{\text{est}} = (1.4 - 7.0) \cdot 10^{-8} M_\odot \text{year}^{-1}$ is broad. Acceptable mod-

els in Moscibrodzka et al. (2009) give \dot{M} from $0.9 \cdot 10^{-8} M_\odot \text{year}^{-1}$ to $12 \cdot 10^{-8} M_\odot \text{year}^{-1}$, which agrees with our range. Dexter et al. (2010) reported 90% confidence interval of \dot{M} for spin $a_* = 0.9$ solutions, while incorporating flow size in χ^2 analysis. Our estimates have somewhat higher accretion rates than the range $\dot{M} = 5_{-2}^{+15} \times 10^{-9} M_\odot \text{year}^{-1}$ (90%) in Dexter et al. (2010), because models with lower spin naturally need higher \dot{M} to fit the data. Note that Dexter et al. (2009) found even lower accretion rate $\dot{M}(a_* = 0.9) = (1.0 - 2.3) \times 10^{-9} M_\odot \text{year}^{-1}$ when they assumed equality of proton and electron temperatures ($T_p = T_e$).

In addition to spin and accretion rate, we can try to estimate the inclination angle θ and electron temperature T_e (T_e is reported at $r = 6M$ in the equatorial plane). Our range is $\theta_{\text{est}} = 42^\circ - 75^\circ$, which agrees with estimates by other groups. Broderick et al. (2009); Dexter et al. (2010) reported $\theta \sim 50^\circ$. Huang et al. (2009a) and Huang et al. (2009b) favor slightly lower $\theta \sim 40^\circ$ and 45° , respectively, but they have large error bars. To estimate T_e , Moscibrodzka et al. (2009) and Dexter et al. (2010) use a constant T_p/T_e , whereas Huang et al. (2009a) and the present work calculated the profile of T_e . In all models, T_e is a shallow function of radius, which made Dexter et al. (2010) estimate a ‘‘common’’ $T_e = (5.4 \pm 3.0) \times 10^{10}$ K (calculated at some distance from the BH center). We measure T_e at $r = 6M$, and we obtain a narrower range (likely owing to fitting of polarized observations) of $T_e = (3.0 - 4.2) \times 10^{10}$ K.

One can use two types of observations to estimate the BH spin axis position angle: the 230 GHz correlated flux and the EVPA. Using the correlated flux gave Broderick et al. (2009) and Dexter et al. (2010) a result of $\text{PA} = (-70^\circ) - (-20^\circ) = (110^\circ) - (160^\circ)$. Using the EVPA data has given slightly different results: Meyer et al. (2007) predicts the range $\text{PA} = 60^\circ - 108^\circ$, whereas Huang gets either $\text{PA} \approx 115^\circ$ (Huang et al. 2009b) or $\text{PA} \approx 140^\circ$ (Huang et al. 2009a). Our values of PA are within the range $85^\circ - 171^\circ$, which is consistent with predictions in Meyer et al. (2007) and with estimates based upon the observed correlated flux. The size of the flow may depend substantially on the luminosity state (Broderick et al. 2009) or the presence of non-thermal structures, spiral waves, and other features. In some astrophysical sources, PA is directly known from spatially resolved jets, and Sgr A* may be one of such sources. A tentative jet feature was revealed in X-rays by Muno et al. (2008) in their fig. 8 showing $\text{PA}_{\text{jet}} = 120^\circ$. This value is close to $\text{PA} = 115.3^\circ$ or $\text{PA} = 120.3^\circ$ for the best fit models with spins $a_* = 0.5$ and $a_* = 0.98$, respectively.

Besides the estimates of accretion rate and flow properties based on the inner flow, there exist estimates based on the outer flow. Shcherbakov & Baganoff (2010) constructed an inflow-outflow model with conduction and stellar winds with radiation matching the X-ray surface brightness profile observed by *Chandra*. Their model⁴ had an accretion rate $\dot{M} = 6 \cdot 10^{-8} M_\odot \text{year}^{-1}$ and electron temperature $T_e = 3.6 \times 10^{10}$ K at $r = 6M$, which is

⁴ Note that gravitational radius is defined as $r_g = 2M$ in Shcherbakov & Baganoff (2010).

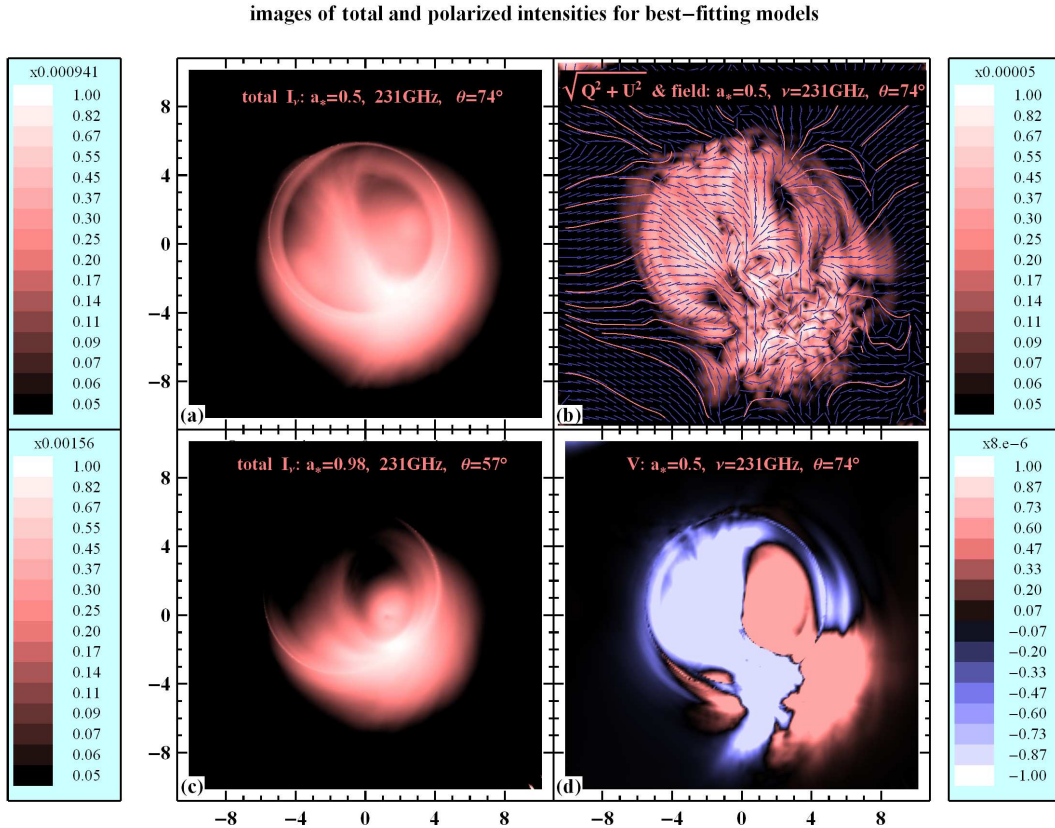


FIG. 11.— Images of polarized intensities for the best fit models: total intensity for spin $a_* = 0.98$ model (lower left); intensities for $a_* = 0.5$ model: total intensity (upper left), linear polarized intensity and streamlines along EVPA (upper right), and circular polarized intensity (lower right). Distances are in the units of BH mass M . Images are rotated in the picture plane to correspond to the best spin PA: PA = 115.3° for the $a_* = 0.5$ model and PA = 120.3° for the $a_* = 0.98$ model. Individual calibration bars are on the sides of corresponding plots. The ill-defined polar region does not contribute significantly to the emission.

consistent with present results. Shcherbakov & Baganoff (2010) constrained the density in the outer-radial flow from X-ray observations, while the present work constrains the density in the inner-radial flow from sub-mm observations. The density profile is then found to be

$$\rho \propto r^{-\beta}, \quad \beta = 0.80 - 0.90. \quad (31)$$

The density power-law index β lies between $\beta = 1.5$ for ADAF flow (Narayan & Yi 1995) and $\beta = 0.5$ for the convection-dominated accretion flow (Narayan, Igumenshchev, & Abramowicz 2000; Quataert & Gruzinov 2000). However, the modification of the power-law index from the steep ADAF profile is likely due to conduction for Sgr A*, not convection (Shcherbakov & Baganoff 2010). Newer GRMHD simulations of radially-extended disks show a comparable power-law index for density (McKinney et al. 2012).

Our dynamical model has limitations and relies on several approximations. More convergence testing, like done in McKinney et al. (2012), is required to ensure the 3D GRMHD simulation results are reliable. The amount of initial magnetic flux and the field geometry might have a pronounced effect on simulation results. For example, magnetically choked accretion flows (MCAF) (Igumenshchev 2008; McKinney et al. 2012) may have more desirable properties (such as larger Faraday rotation as discussed related to Figure 9) for Sgr A* compared to MRI-dominated disks described in the present

work. The dependence of the estimated accretion flow and the BH parameters on the simulation type and the initial setup should be carefully explored in future works. The polarization is expected to be able to best highlight changes in the magnetic field geometry and strength, and so our work is an important stepping stone to distinguish whether Sgr A* is a classical MRI-dominated disk or an MCAF.

The limited dynamical range of our simulations leads to another caveat. We fix electron density n_e and temperatures T_p and T_e in the outer flow and extend them down to the event horizon. The slopes of these quantities break at $25M$ radius, where the power law radial extrapolation starts. Thus, the density and temperature slopes in the inner flow may need to be determined more self-consistently. Future simulations will need to cover a larger range of radii and plasma physics effects, such as conduction (Johnson & Quataert 2007; Sharma et al. 2008; Shcherbakov & Baganoff 2010). Simulations with larger outer radial boundaries that are run for longer will also help to fit the Faraday rotation, which happens for the present models partially outside of the simulated domain. A proper simulation of the polar region of the flow may be important as well. At present, we artificially limit the lowest density and highest temperature there. If we do not, then numerical artifacts associated with excessive numerical dissipation and heating appear (similar to those in Moscibrodzka et al. 2009).

We found the lowest χ^2/dof for the model with spin $a_* = 0.5$, whereas other groups found $a_* = 0$ and $a_* = 0.9$ to provide the best fits in their modeling. So, there still appears to be no reliable estimate of BH spin for SgrA*. One common shortcoming of recent papers is the use of thermal electron distribution. If non-thermal electrons provide most of the energy for the sub-mm peak, then this would invalidate all prior spin estimates (Shcherbakov & Huang 2011).

The radiative transfer we performed has its shortcomings. The emissivities in our special synchrotron approximation provide, e.g., 2% agreement with exact emissivities (Leung, Gammie & Noble 2011; Shcherbakov & Huang 2011) for $b = 20$ G, $\theta_B = 1$ rad, $T_e = 6.9 \cdot 10^9$ K, and observed frequency $\nu = 100$ GHz. Agreement is better for larger T_e . Non-polarized radiative transfer methods (Moscibrodzka et al. 2009; Dexter et al. 2010) have an intrinsic error that is comparable with our polarized radiative transfer method for the same total emissivity ε_I , but the error is still 1 – 5%.

There are other unaccounted sources of error. The mass of the BH in the Galactic Center is known to within 10% (Ghez et al. 2008; Gillessen et al. 2009) and the distance is known to 5%. We do not expect these uncertainties to lead to significant changes in our predictions. A shift to slightly lower spin may be able to mimic the effect of smaller BH or a BH at larger distance.

An improvement in observations can lead to further insights on the flow and black hole parameters. For example, the detailed comparison of flux, LP, and CP curves in Figure 7 shows that the models with different spins have discrepancies at frequencies not yet probed by observations. In particular, the CP fractions at 88 GHz and 690 GHz are different. The EVPA data need improvement as well. EVPA observations are available at 230 GHz and 349 GHz, but these frequencies are affected by Faraday rotation. The observations at higher frequency, where the Faraday rotation effect is weaker, should provide a better estimate of BH spin axis PA. Another important quantity, LP at 88 GHz, has a largely unknown value. Its observations are reported in 2 papers. Variations in simulated LP(88GHz) are large between the best fit models (see Figure 7). Refinement of the observed mean LP(88GHz) could potentially help discriminate between different spins. A measurement of the emitting region size or the correlated flux is also promising. Despite the correlated flux at 230 GHz being measured at the SMT-JCMT 3.5G λ baseline, the statistics of this measurement need to be improved towards being comparable with the statistics of total flux. The corre-

lated flux observations are currently being accumulated (Fish et al. 2011). The correlated flux at this baseline is exponentially sensitive to the physical flow size. As a caveat, the conclusion on image sizes may depend on the behavior of matter in the ill-defined polar regions. Our models do not exhibit significant emission from high latitudes at 230 GHz (see Figure 11) or anywhere above 88 GHz.

Future work should incorporate rigorous statistical analysis, and such analysis should include temporal information from the observations. The time variability properties can be found from the simulations and compared to the observed ones. In particular, “jet lags” (Yusef-Zadeh et al. 2008; Maitra, Markoff & Falcke 2009) and quasi-periodic oscillations (QPOs) (Genzel et al. 2003; Eckart et al. 2006; Miyoshi 2010) should be investigated using the simulations (Dolence et al. 2012). Also, future 3D GRMHD simulations will model more radially extended flows, account for ADAF/ADIOS type scale-heights of $|h/r| \sim 1$, capture outflows, and account for the effects of accumulated magnetic flux near the black hole (McKinney et al. 2012). Lastly, for the radiative transfer, adding Comptonization would be one way to test the quiescent X-ray luminosity $L \approx 4 \cdot 10^{32} \text{erg s}^{-1}$ within 2 – 10 keV (Shcherbakov & Baganoff 2010).

8. ACKNOWLEDGEMENTS

The authors are grateful to Lei Huang for checking various emissivity prescriptions, to Ramesh Narayan for extensive discussions and comments, to Avi Loeb, Avery Broderick, James Moran, Alexander Tchekhovskoy, Cole Miller, Julian Krolik, Steven Cranmer for insightful comments and Jim Stone for encouragement with self-consistent radiative transfer. We thank the anonymous referees for their extensive feedback, which helped to improve the manuscript. The numerical simulations and the radiative transfer calculations in this paper were partially run on the Odyssey cluster supported by the FAS Sciences Division Research Computing Group at Harvard, Deepthought cluster at the University of Maryland, and were partially supported by NSF through TeraGrid resources provided by NCSA (Abe), LONI (QueenBee), and NICS (Kraken) under grant numbers TG-AST080025N and TG-AST080026N. The paper is partially supported by NASA grants NNX08AX04H (RVS&Ramesh Narayan), NNX08AH32G (Ramesh Narayan), NASA Hubble Fellowship grant HST-HF-51298.01 (RVS), NSF Graduate Research Fellowship (RFP), and NASA Chandra Fellowship PF7-80048 (JCM).

REFERENCES

- Aitken, D. K., Greaves, J., Chrysostomou, A., Jenness, T., Holland, W., Hough, J. H., Pierce-Price, D., Richer, J. 2000, *ApJ*, 534, 173
- An, T., Goss, W. M., Zhao, J.-H., Hong, X. Y., Roy, S., Rao, A. P., Shen, Z.-Q. 2005, *ApJ*, 634, 49
- Andrae, R., Schulze-Hartung, T., Melchior, P. 2010, astro-ph/1012.3754
- Baganoff, F. K., et al. 2001, *Nature*, 413, 45
- Baganoff, F. K., et al. 2003, *ApJ*, 591, 891
- Balbus, S. A., & Hawley, J. F. 1998, *Reviews of Modern Physics*, 70, 1
- Beckwith K., Hawley J. F., Krolik J. H., 2008a, *ApJ*, 678,1180
- Berger, J. O. 1985, “Statistical Decision Theory and Bayesian Analysis”, (New York: Springer-Verlag)
- Blandford, R. D., & Begelman, M. C. 1999, *MNRAS*, 303L, 1
- Bower, G. C., Falcke, H., Backer, D. C. 1999a, *ApJ*, 523, L29
- Bower, G. C., Wright, M. C. H., Backer, D. C., Falcke, H. 1999b, *ApJ*, 527, 851
- Bower, G. C., Wright, M. C. H., Falcke, H., Backer, D. C. 2001, *ApJ*, 555, 103
- Bower, G. C., Falcke, H., Sault, R. J., Backer, D. C. 2002, *ApJ*, 571, 843
- Bower, G. C., Wright, M. C. H., Falcke, H., Backer, D. C. 2003, *ApJ*, 588, 331

- Bower, G. C., Falcke, H., Wright, M. C., Backer, & Donald C. 2005, *ApJ*, 618, 29
- Broderick, A. E., Fish, V. L., Doeleman, S. S., Loeb, A. 2009, *ApJ*, 697, 45
- Broderick, A. E., Fish, V. L., Doeleman, S. S., Loeb, A. 2010, *astro-ph/1011.2770*
- Chakrabarti S. K., 1985a, *ApJ*, 288, 1
- Chakrabarti S. K., 1985b, *ApJ*, 294, 383
- Chan, C.-K., Liu, S., Fryer, C. L., Psaltis, D., O’zel, F., Rockefeller, G., Melia, Fulvio 2009, *ApJ*, 701, 521
- De Villiers J.-P., Hawley J. F., Krolik J. H., 2003, *ApJ*, 599, 1238
- Dexter, J., Agol, E., Fragile, P. C. 2009, *ApJ*, 703, 142
- Dexter, J., Agol, E., Fragile, P. C., McKinney, J. C. 2010, *ApJ*, 717, 1092
- Dolence, J. C., Gammie, C. F., Moscibrodzka, M., Leung, P. K. 2009, *ApJS*, 184, 387
- Dolence, J. C., Gammie, C. F., Shiokawa, H., Noble, S. C. 2012, *ApJ*, 746, 10
- Doeleman S. S. et al 2001, *AJ*, 121, 2610
- Doeleman, S. S. et al. 2008, *Nature*, 455, 78
- Eckart, A., Schödel, R., Meyer, L., Trippe, S., Ott, T., Genzel, R. 2006, *A&A*, 455, 1
- Falcke, H., Goss, W. M., Matsuo, H., Teuben, P., Zhao, J.-H., Zylka, R. 1998, *ApJ*, 499, 731
- Fish, V. L., Broderick, A. E., Doeleman, S. S., Loeb, A. 2009, *ApJ*, 692, L14
- Fish, V. L., et al. 2011, *ApJ*, 727, 36
- Fragile, P. C., Lindner, C. C., Anninos, P., & Salmonson, J. D. 2009, *ApJ*, 691, 482
- Fuerst, S. V., Wu, K. 2004, *A&A*, 424, 733
- Gammie, C. F., McKinney, J. C., Toth, G. 2003, *ApJ*, 589, 444
- Gammie, C. F., Shapiro, S. L., McKinney, J. C. 2004, *ApJ*, 602, 312
- Ghez, A. M., et al. 2008, *ApJ*, 689, 1044
- Ghosh, S., & Mukhopadhyay, B. 2007, *ApJ*, 667, 367
- Genzel, R., Schödel, R., Ott, T., Eckart, A., Alexander, T., Lacombe, F., Rouan, D., Aschenbach B. 2003, *Nature*, 425, 934
- Gillessen, S., Eisenhauer, F., Fritz, T. K., Bartko, H., Dodds-Eden, K., Pfuhl, O., Ott, T., Genzel, R. 2009, *ApJ*, 707, 114
- Goldston, J. E., Quataert, E., Igumenshchev, I. V. 2005, *ApJ*, 621, 785
- Hamaker J. P., Bregman J. D. 1996, *A & AS*, 117, 161
- Hawley, J. F., Guan, X., Krolik, J. H. 2011, *ApJ*, 738, 84
- Herrnstein, R. M., Zhao, J.-H., Bower, G. C., Goss, W. M. 2004, *AJ*, 127, 3399
- Hide, R., Palmer, T. N. 1982, *Geophys. and Astrophys. Fluid Dynamics*, 19, 301
- Homan, D. C., Lister, M. L., Aller, H. D., Aller, M. F., Wardle, J. F. C. 2009, *ApJ*, 696, 328
- Huang, L., Liu, S., Shen, Z.-Q., Cai, M. J., Li, H., & Fryer, C. L. 2008, *ApJ*, 676L, 119
- Huang, L., Liu, S., Shen, Z.-Q., Yuan, Y.-F., Cai, M. J., Li, H., & Fryer, C. L. 2009a, *ApJ*, 703, 557
- Huang, L., Takahashi, R., Shen, Z.-Q. 2009b, *ApJ*, 706, 960
- Igumenshchev, I. V. 2008, *ApJ*, 677, 317
- Jaynes, E. T., Bretthorst, G. L. 2003, "Probability Theory", (Cambridge: Cambridge University Press)
- Johnson, B. M., Quataert, E. 2007, *ApJ*, 660, 1273
- Komissarov S. S., McKinney J. C., 2007, *MNRAS*, 377, L49
- Krichbaum T. P. 1998, *A&A*, 335, L106
- Krichbaum, T. P., Graham, D. A., Bremer, M., Alef, W., Witzel, A., Zensus, J. A., Eckart, A. 2006, *JPhCS*, 54, 328
- Legg, M. P. C., Westfold, K. C., 1968, *ApJ*, 154, 499
- Leung, P. K., Gammie, C. F., Noble S. C. 2011, *ApJ*, 737, 21
- Li, J., Shen, Z.-Q., Miyazaki, A., Huang, L., Sault, R. J., Miyoshi, M., Tsuboi, M., Tsutsumi, T. 2008, *JPhCS*, 131, 2007
- Lo, K. Y., Shen, Z.-Q., Zhao, J.-H., Ho, P. T. P. 1998, *ApJ*, 508, L61
- Lu, R.-S., Krichbaum, T. P., Eckart, A., König, S., Kunneriath, D., Witzel, G., Witzel, A., Zensus, J. A. 2008, *JPhCS*, 131, 2059
- Macquart, J.-P., Bower, G. C., Wright, M. C. H., Backer, Donald C., Falcke, H. 2006, *ApJ*, 646, L111
- Mahadevan, R. 1998, *Nature*, 394, 651
- Maitra, D., Markoff, S., Falcke, H. 2009, *A&A*, 508, 13
- Marrone, D. P., Moran, J. M., Zhao, J.-H., Rao, R. 2006a, *JPhCS*, 54, 354
- Marrone, D. P., Moran, J. M., Zhao, J.-H., Rao, R. 2006b, *ApJ*, 640, 308
- Marrone, D. P., Moran, J. M., Zhao, J., & Rao R., 2007, *ApJ*, 654L, 57
- Marrone D. P., et al. 2008, *ApJ*, 682, 373
- Mauerhan, J. C., Morris, M., Walter, F., Baganoff, F. K. 2005, *ApJ*, 623, 25
- McKinney, J. C., & Gammie, C. F. 2004, *ApJ*, 611, 977
- McKinney, J. C. 2006, *MNRAS*, 367, 1797
- McKinney, J. C. 2006, *MNRAS*, 368, 1561
- McKinney, J. C., & Blandford, R. D. 2009, *MNRAS*, 394, L126
- McKinney J. C., Narayan R., 2007a, *MNRAS*, 375, 513
- McKinney J. C., Narayan R., 2007b, *MNRAS*, 375, 531
- McKinney, J. C., Tchekhovskoy, A., & Blandford, R. D. 2012, *arXiv:1201.4163*
- Melrose, D. B. 1971, *Ap&SS*, 12, 172
- Meyer, L., Schödel, R., Eckart, A., Duschl, W. J., Karas, V., Dovčiak, M. 2007, *A&A*, 473, 707
- Mignone, A., McKinney, J. C. 2007, *MNRAS*, 378, 1118
- Miyazaki, A., Tsutsumi, T., Tsuboi, M. 2004, *ApJ*, 611, 97
- Miyoshi, M., Shen, Z.-Q., Oyama, T., Takahashi, R., Kato, Y. 2010, *astro-ph/0906.5511*
- Moscibrodzka, M., Gammie, C. F., Dolence, J. C., Shiokawa, H., Leung, P. K. 2009 *ApJ*, 706, 497
- Muno, M. P., et al. 2008, *ApJ*, 673, 251
- Munoz, D. J., Marrone, D. P., Moran, J. M. 2009, *Bulletin of the AAS*, 41, 761
- Munoz, D. J., Marrone, D. P.; Moran, J. M., Rao, R. 2011, *ApJ*, submitted
- Narayan, R., & Yi, I. 1995, *ApJ*, 452, 710
- Narayan, R., Yi, I., Mahadevan, R. 1995, *Nature*, 374, 623
- Narayan, R., Mahadevan, R., Grindlay, J. E., Popham, R. G., Gammie, C. 1998, *ApJ*, 492, 554
- Narayan, R., Igumenshchev, I. V., & Abramowicz, M. A. 2000, *ApJ*, 539, 798
- Noble, S. C., Gammie, C. F., McKinney, J. C., Del Zanna, L. 2006, *ApJ*, 641, 626
- Noble, S. C., Krolik, J. H. 2009, *ApJ*, 703, 964
- Özel, F., Psaltis, D., Narayan, R. 2000, *ApJ*, 541, 234
- Pacholczyk, A. G. 1970, "Radio astrophysics. Nonthermal processes in galactic and extragalactic sources", (Freeman: San Francisco)
- Penna, R. F., McKinney, J. C., Narayan, R., Tchekhovskoy, A., Shafee, R., McClintock, J. E. 2010, *MNRAS*, 408, 752
- Quataert, E., & Gruzinov, A. 2000, *ApJ*, 539, 809d
- Reid, M. J., Broderick, A. E., Loeb, A., Honma, M., Brunthaler, A. 2008, *ApJ*, 682, 1041
- Rybicki, G. B., & Lightman, A. P. 1979, "Radiative processes in astrophysics," (Wiley-Interscience: New York)
- Sazonov, V. N. 1969, *Soviet Astronomy*, 13, 396
- Serabyn, E., Carlstrom, J., Lay, O., Lis, D. C., Hunter, T. R., Lacy, J. H. 1997, *ApJ*, 490, L77
- Shafee R., McKinney J. C., Narayan R., Tchekhovskoy A., Gammie C. F., McClintock J. E., 2008, *ApJ*, 687, L25
- Sharma, P., Quataert, E., Hammett, G. W., & Stone, J. M. 2007, *ApJ*, 667, 714
- Sharma, P., Quataert, E., Stone, J. M. 2008, *MNRAS*, 389, 1815
- Shcherbakov, R. V. 2008, *ApJ*, 688, 695
- Shcherbakov, R. V., Baganoff F. K. 2010, *ApJ*, 716, 504
- Shcherbakov, R. V., Huang, L. 2010, *MNRAS*, 410, 1052
- Shen, Z.-Q., Lo, K. Y., Liang, M.-C., Ho, P. T. P., Zhao, J.-H. 2005, *Nature*, 438, 62
- Shkarofsky, I. P., Johnston, T. W., Bachynski, M. P. 1966, "The particle kinetics of plasma," (Addison-Wesley Publishing Company: London)
- Tchekhovskoy, A., McKinney, J. C., Narayan, R. 2007, *MNRAS*, 379, 469
- Yuan, F., Markoff, S., & Falcke, H. 2002, *A&A*, 383, 854
- Yuan, F., Quataert, E., Narayan, R. 2004, *ApJ*, 606, 894
- Yusef-Zadeh, F., Wardle, M., Cotton, W. D., Heinke, C. O., Roberts, D. A. 2007, *ApJ*, 668, 47
- Yusef-Zadeh, F., Wardle, M., Heinke, C., Dowell, C. D., Roberts, D., Baganoff, F. K., Cotton, W. 2008, *ApJ*, 682, 361
- Yusef-Zadeh, F., et al. 2009, *ApJ*, 706, 348

Zhao, J.-H., Young, K. H., Herrnstein, R. M., Ho, P. T. P.,
Tsutsumi, T., Lo, K. Y., Goss, W. M., Bower, G. C. 2003, ApJ,
586, 29

APPENDIX

RADIATIVE TRANSFER CONVERGENCE

We have devised a novel code for GR polarized radiative transfer. As with any new code, we need to conduct a set of convergence tests to ensure it works accurately. First, we need to come up with metrics for assessing accuracy. In the present paper we model fluxes at 7 frequencies between 88 GHz and 857 GHz, LP fractions at 3 frequencies and CP fractions at 2 frequencies and define χ^2 as to characterize the goodness of fit. We employ a similar quantity χ_H^2/dof to characterize the accuracy of radiative transfer. We define

$$\chi_H^2/\text{dof} = \frac{1}{9} \sum_{i=1}^{12} \frac{(Q_{i,1} - Q_{i,2})^2}{\sigma(Q)^2}, \quad (\text{A1})$$

where $Q_{i,1}$ are simulated polarized fluxes for one set of radiative transfer parameters and $Q_{i,2}$ are the fluxes for another set. The errors $\sigma(Q)$ are the observed errors of the mean, and the index i runs through all fitted fluxes, LP, and CP fractions. When one of the models fits the data exactly, then χ_H^2/dof coincides with χ^2/dof . We vary the following radiative transfer and dynamical model parameters:

- number of points P_N along North-South axis and along East-West axis in the picture plane,
- distance from the center P_{ss} measured in horizon radii r_H , where radiative transfer starts,
- dimensionless scale P_{fact} of the integration region in the picture plane,
- number of simulated spectra N_{periods} for a single model to compute the mean spectrum,
- time interval Δt of simultaneous propagation of rays and evolution of numerical simulations,
- extension power-law slope of density profile P_{rhopo} ,
- extension slope of temperature profile P_{Upo} ,
- extension slope of magnetic field profile P_{Bpo} .

Since fluctuations and differences in χ^2/dof between different models reach 1, then values $\chi_H^2/\text{dof} \lesssim 0.1$ are acceptable, but, in general, we strive for $\chi_H^2/\text{dof} < 0.02$. We set constant P_{fact} , P_{ss} , P_{snxy} for all radiative transfer computations, but we cannot check the code accuracy for all models. We check the convergence a posteriori for the best fit model at each spin value.

We find values of parameters by trial-and-error. The resulting set has $P_{\text{fact}} = 1$, $P_{\text{ss}} = 1.01r_H$, $P_{\text{snxy}} = 111$, $N_{\text{periods}} = 21$, $\Delta t = 120M$. The values of P_{rhopo} and P_{Upo} are fixed by extensions to large radii of temperature and density in the inner flow.

The tests and the values of χ_H^2/dof are summarized in Table 3. The second column describes the test. In particular, $P_{\text{fact}} : 1 \rightarrow 0.8$ means that we test convergence of the integration region relative size. We change one parameter at a time. Since the power-law slopes P_{rhopo} and P_{Upo} can vary from model to model, we change them in such a way that P_{rhopo} is increased by 0.2 and P_{Upo} is decreased by 0.1. We also estimate the influence of magnetic field extension power-law slope P_{Bpo} by making it shallower from $(r/M)^{-1.0}$ to $(r/M)^{-0.8}$. We chose to test relatively small variations $\Delta P_{\text{rhopo}} = 0.2$ and $\Delta P_{\text{Upo}} = 0.1$, because density and temperature at $r_{\text{out}} = 3 \cdot 10^5 M$ are known to within a factor of several (Baganoff et al. 2003; Shcherbakov & Baganoff 2010), while these variations correspond to changes by factors of 7 and 2.5 in density and temperature, respectively, at r_{out} .

The results of the tests are as follows. The first 11 tests represent variations of radiative transfer parameters and last 3 tests explore the variations of power-law extension slopes. Tests 1 – 4 produce small χ_H^2/dof , so that P_N can be lowered and P_{ss} can be increased. The changes in the integration region scale (P_{fact}) result in high $\chi_H^2/\text{dof} \approx 0.07$, as indicated by tests 5 and 6. Low P_{fact} leads to systematic underproduction of total flux, whereas high P_{fact} mainly leads to different LP fractions. Test 7 results in high $\chi_H^2/\text{dof} \approx 0.4$, so that a small number of simulated spectra (e.g. $N_{\text{periods}} = 11$) cannot be justified. Lower values $\chi_H^2/\text{dof} \approx 0.13$ attained in test 8 indicate that $N_{\text{periods}} = 21$ periods might be acceptable. With tests 9 – 11, we tested variations in the time interval Δt of simultaneous propagation of rays and evolution of numerical simulations. It is expected that longer intervals lead to convergence. However, switching from $\Delta t = 120M$ to $\Delta t = 180M$ and switching $\Delta t = 80M$ to $\Delta t = 120M$ both lead to $\chi_H^2/\text{dof} \lesssim 0.1$. Since these values of χ_H^2/dof are acceptable, we implement $\Delta t = 120M$ for radiative transfer runs. As elucidated by test 11, freezing simulations in time leads to $\chi_H^2/\text{dof} \approx 0.5$, which is too high. Thus, conducting radiative transfer over frozen simulation snapshots is not acceptable. Changes in extension slopes of density and temperature (tests 12 and

TABLE 3

VALUES OF χ_H^2/dof FOR RADIATIVE TRANSFER CONVERGENCE TESTS AND SENSITIVITY TO MODEL PARAMETERS TESTS FOR BEST FIT MODELS.

Number	Description	spin $a_* = 0$	spin $a_* = 0.5$	spin $a_* = 0.7$	spin $a_* = 0.9$	spin $a_* = 0.98$
1	$P_N : 75 \rightarrow 111$	0.00081	0.00138	0.00101	0.00047	0.01175
2	$P_N : 111 \rightarrow 161$	0.00017	0.00072	0.00018	0.00007	0.00084
3	$P_{ss} : 1.003r_H \rightarrow 1.01r_H$	0.00036	0.00059	0.00110	0.00095	0.00051
4	$P_{ss} : 1.01r_H \rightarrow 1.03r_H$	0.00778	0.00982	0.01616	0.01468	0.00920
5	$P_{\text{fact}} : 0.8 \rightarrow 1.0$	0.01358	0.07278	0.06905	0.02893	0.02686
6	$P_{\text{fact}} : 1.0 \rightarrow 1.2$	0.00087	0.05532	0.07173	0.02681	0.03534
7	$N_{\text{periods}} : 11 \rightarrow 21$	0.15665	0.40611	0.12233	0.21397	0.13588
8	$N_{\text{periods}} : 21 \rightarrow 41$	0.02474	0.04505	0.13244	0.02684	0.04834
9	interval $\Delta t: 120M \rightarrow 180M$	0.06987	0.06851	0.13549	0.02948	0.10979
10	interval $\Delta t: 80M \rightarrow 120M$	0.09095	0.04103	0.03094	0.03881	0.06246
11	interval $\Delta t: 0M \rightarrow 120M$	0.09051	0.35296	0.53045	0.02731	0.07881
12	$P_{\text{rhopo}} : Q \rightarrow Q+ = 0.2$	0.04493	0.04057	0.03134	0.01587	0.05241
13	$P_{\text{Upo}} : Q \rightarrow Q- = 0.1$	0.01200	0.02726	0.00977	0.01088	0.04174
14	$P_{\text{Bpo}} : -1.0 \rightarrow -0.8$	0.02401	1.05214	0.15156	0.05486	0.04941

13) result in small $\chi_H^2/\text{dof} \lesssim 0.05$. Variations of magnetic field slope (test 14) lead to large $\chi_H^2/\text{dof} \approx 1$, which means the modifications of \mathbf{b} extensions will change the best fits. Extensions as shallow as $|\mathbf{b}| \propto (r/M)^{-0.5}$ may provide better fits to Faraday rotation measure and should be carefully explored. Various extensions of the fluid velocity lead to practically the same polarized intensities and are not included in tests.